

# 1 A 20-year (1998–2017) global sea surface dimethyl sulfide gridded 2 dataset with daily resolution

3 Shengqian Zhou<sup>1</sup>, Ying Chen<sup>1,2,3</sup>, Shan Huang<sup>4,5</sup>, Xianda Gong<sup>6,7</sup>, Guipeng Yang<sup>8,9,10</sup>, Honghai  
4 Zhang<sup>8,9,10</sup>, Hartmut Herrmann<sup>5</sup>, Alfred Wiedensohler<sup>5</sup>, Laurent Poulaïn<sup>5</sup>, Yan Zhang<sup>1,2</sup>, Fanghui Wang<sup>1</sup>,  
5 Zongjun Xu<sup>1</sup>, Ke Yan<sup>1</sup>

6 <sup>1</sup>Shanghai Key Laboratory of Atmospheric Particle Pollution Prevention, Department of Environmental Science &  
7 Engineering, Fudan University, Shanghai, 200438, China

8 <sup>2</sup>Institute of Eco-Chongming (IEC), National Observations and Research Station for Wetland Ecosystems of the Yangtze  
9 Estuary, Shanghai, 200062, China

10 <sup>3</sup>Institute of Atmospheric Sciences, Fudan University, Shanghai 200438, China

11 <sup>4</sup>Institute for Environmental and Climate Research, Jinan University, Guangzhou, 511443, China

12 <sup>5</sup>Leibniz Institute for Tropospheric Research, Leipzig, 04318, Germany

13 <sup>6</sup>Research Center for Industries of the Future, Westlake University, Hangzhou, 310030, China

14 <sup>7</sup>Key Laboratory of Coastal Environment and Resources of Zhejiang Province, School of Engineering, Westlake University,  
15 Hangzhou, 310030, China

16 <sup>8</sup>Frontiers Science Center for Deep Ocean Multispheres and Earth System, and Key Laboratory of Marine Chemistry Theory  
17 and Technology, Ministry of Education, Ocean University of China, Qingdao, 266100, China

18 <sup>9</sup>Laboratory for Marine Ecology and Environmental Science, Qingdao National Laboratory for Marine Science and  
19 Technology, Qingdao, 266071, China

20 <sup>10</sup>College of Chemistry and Chemical Engineering, Ocean University of China, Qingdao, 266100, China

21 *Correspondence to:* Ying Chen (yingchen@fudan.edu.cn)

22 **Abstract.** The oceanic emission of dimethyl sulfide (DMS) plays a vital role in the Earth's climate system and constitutes a  
23 substantial source of uncertainty in evaluating aerosol radiative forcing. Currently, the widely used monthly climatology of  
24 sea surface DMS concentration falls short of meeting the requirement for accurately simulating DMS-derived aerosols by  
25 chemical transport models. Hence, there is an urgent need for a high-resolution, multi-year global sea surface DMS dataset.

26 Here we develop an artificial neural network ensemble model using 9 environmental factors as input features, which ~~exhibits~~  
27 ~~high accuracy and generalization in predicting DMS concentrations~~  
28 ~~well captures the variabilities of DMS concentration across different oceanic regions~~.

29 Subsequently, a global sea surface DMS concentration and flux dataset ( $1^\circ \times 1^\circ$ ) with daily resolution  
30 spanning from 1998 to 2017 is established. According to this dataset, the global annual average concentration was  $\sim 1.72-71$

31 nM, and the annual total emission was  $\sim 17.02$  TgS yr<sup>-1</sup>, with  $\sim 64.60\%$  originating from the southern hemisphere. While overall  
32 seasonal variations are consistent with previous DMS climatologies, notable differences exist in regional-scale spatial  
33 distributions. The new dataset enables further investigations into daily and decadal variations. Throughout the period 1998–

34 2017, the global annual average concentration exhibited a slight decrease, while total emissions showed no significant trend.  
35 The DMS flux from our dataset showed a stronger correlation with observed atmospheric methanesulfonic acid concentration  
36 compared to those from previous monthly climatologies. Therefore, it can serve as an improved emission inventory of oceanic  
DMS and has the potential to enhance the simulation of DMS-derived aerosols and associated radiative effects. The new DMS

37 gridded products are available at <https://doi.org/10.5281/zenodo.1187990><https://zenodo.org/records/10906101> (Zhou et al.,  
38 2024).

## 39 **1 Introduction**

40 Dimethyl sulfide (DMS), primarily produced by ocean biota, accounts for more than half of natural sulfur emissions and  
41 significantly contributes to sulfur dioxide in the troposphere (Sheng et al., 2015; Andreae, 1990), which can be oxidized to  
42 sulfuric acid and form sulfate aerosols (Barnes et al., 2006; Hoffmann et al., 2016). Sulfate aerosols play an important role in  
43 climate systems by scattering solar radiation, changing cloud condensation nuclei (CCN) population, and altering cloud  
44 properties (Masson-Delmotte et al., 2021). Recent studies have proven that CCN over the remote ocean and polar regions are  
45 primarily composed of non-sea-salt sulfate ( $\text{nss-SO}_4^{2-}$ ) (Quinn et al., 2017; Park et al., 2021). Given the weak influence of  
46 anthropogenic  $\text{SO}_2$  over open oceans, marine biogenic DMS emerges as a crucial source of  $\text{nss-SO}_4^{2-}$ , regulating oceanic  
47 climate (McCoy et al., 2015). Accordingly, DMS has been suggested to be the key substance in the postulated feedback loop  
48 of marine phytoplankton to climate warming (the “CLAW” hypothesis) (Charlson et al., 1987), albeit facing several  
49 controversies (Quinn and Bates, 2011). To accurately simulate the climate effects of DMS-derived aerosols, high-fidelity and  
50 high-resolution data on sea surface DMS concentrations and emission fluxes are required, along with further exploration of  
51 complex atmospheric chemical and physical processes (Hoffmann et al., 2016; Novak et al., 2021). It has been indicated that  
52 the uncertainty in DMS emission flux is the second largest contributor to the overall uncertainty associated with natural  
53 aerosols in evaluating the aerosol indirect radiative forcing (Carslaw et al., 2013). Therefore, understanding the spatiotemporal  
54 variations of DMS in global oceans is currently an important task.

55 There are complex production and consumption mechanisms of DMS in the upper ocean, which makes it difficult to well  
56 capture the dynamics and distributions of sea surface DMS across different regions. Dimethylsulfoniopropionate (DMSP), the  
57 major precursor of DMS, is synthesized mainly by phytoplankton in the photic zone and plays a variety of physiological  
58 functions in algal cells (Stefels, 2000; Sunda et al., 2002; McParland and Levine, 2018). The DMSP yield varies significantly  
59 among algal species (Stefels et al., 2007; Keller et al., 1989), and DMS can be produced through DMSP intracellular and  
60 extracellular cleavage by both algae and bacteria (Alcolombri et al., 2015; Zhang et al., 2019). Therefore, the oceanic DMS  
61 produced via multiple pathways can be affected by many biotic and abiotic factors, including temperature, salinity, solar  
62 radiation, mixed layer depth, nutrients, oxygen, acidity, etc. (Simó and Pedrós-Alió, 1999a; Vallina and Simó, 2007; Stefels,  
63 2000; Zindler et al., 2014; Six et al., 2013; Omori et al., 2015; Stefels et al., 2007). In addition, seawater DMS undergoes  
64 various removal pathways (bacterial consumption, photodegradation, sea-to-air ventilation, etc.), further complicating its  
65 cycling (Stefels et al., 2007; Galí and Simó, 2015; Hopkins et al., 2023). Therefore, although previous studies have developed  
66 several empirical algorithms (Simó and Dachs, 2002; Belviso et al., 2004b; Vallina and Simó, 2007) and process-embedded  
67 prognostic models (Kloster et al., 2006; Vogt et al., 2010; Belviso et al., 2011; Wang et al., 2015) based on relevant variables

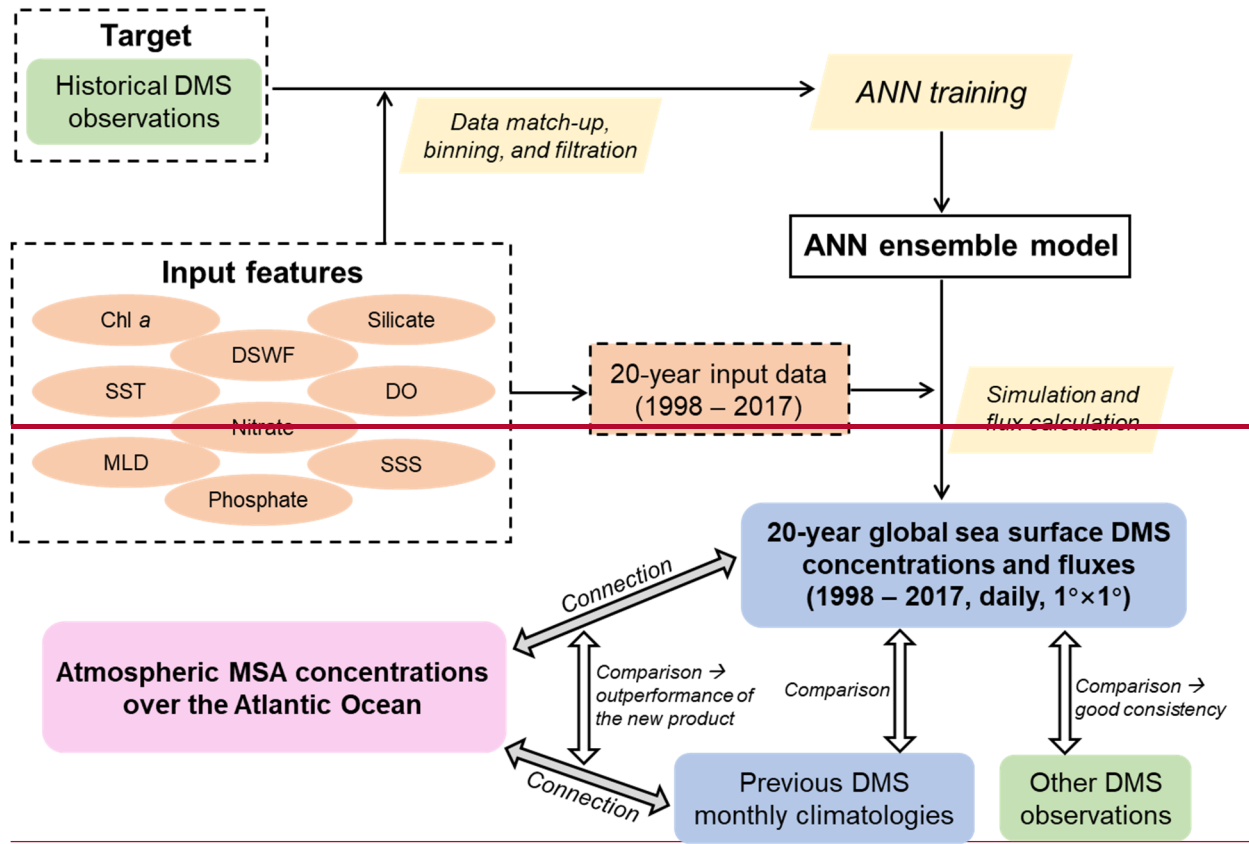
68 (mixed layer depth, chlorophyll *a*, nutrients, radiation, phytoplankton group, etc.) to estimate the distribution of DMS, their  
69 results showed significantly different patterns and inconsistency with observations in many regions (Tesdal et al., 2016;  
70 Belviso et al., 2004a). Recently, Galí et al. (2018) developed a new empirical algorithm following a parameterization of DMSP  
71 (Galí et al., 2015). The estimated DMS field exhibited a generally higher consistency with observations than those derived  
72 from previous algorithms SD02 (Simó and Dachs, 2002) and VS07 (Vallina and Simó, 2007), but this method did not consider  
73 the influences of nutrients and still exhibited substantial biases in certain regions (e.g., near the Antarctic).

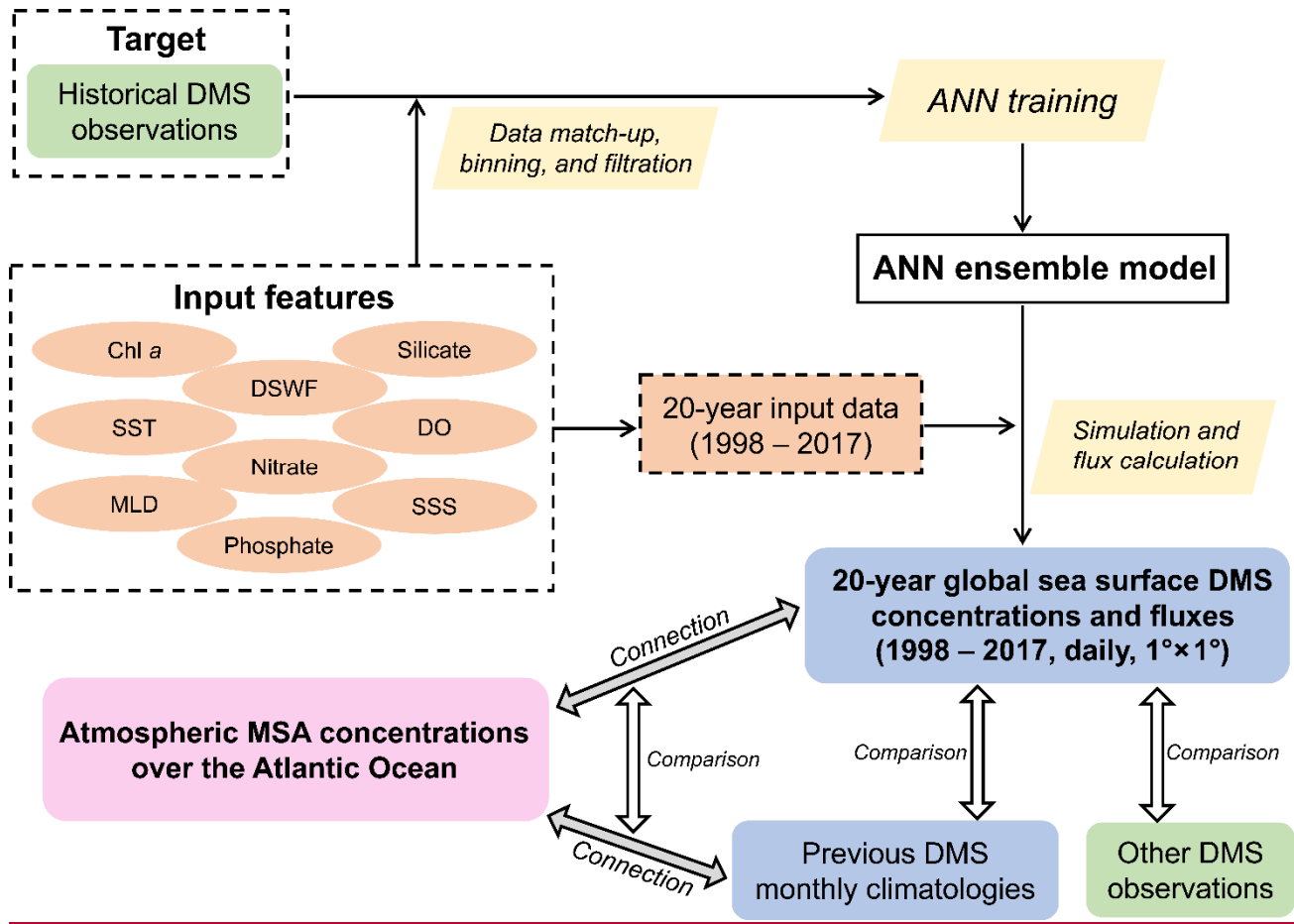
74 Since Lovelock et al. (1972) first discovered the ubiquitous presence of DMS in seawater, numerous observations of sea  
75 surface DMS have been conducted worldwide, yielding a substantial volume of observational data to date. Based on these  
76 worldwide measurements, monthly climatology of global DMS can be generated through interpolation and extrapolation  
77 (Hulswar et al., 2022; Kettle et al., 1999; Lana et al., 2011). The latest version incorporated 873,539 raw observations (48,898  
78 after data filtration and unification for climatology development), and the estimated global annual mean concentration and  
79 total flux are 2.26 nM and 27.1 TgS yr<sup>-1</sup>, respectively (Hulswar et al., 2022). However, despite the abundance of data,  
80 significant spatial and temporal disparities persist, potentially introducing large uncertainties in regions or periods with sparse  
81 observations. Furthermore, the observational data from different years within a particular month were combined together for  
82 interpolation and extrapolation, and the interannual variations cannot be investigated by this approach.

83 In recent years, the application of data-driven approaches like machine learning to Earth system science has drawn more and  
84 more attention. Compared with traditional approaches, machine learning explores larger function space and captures more  
85 hidden information from the big data, hence it often provides a better prediction performance (Reichstein et al., 2019; Zheng  
86 et al., 2020; Bergen et al., 2019). For instance, a recent study demonstrated that artificial neural network (ANN) can capture  
87 much more (~66%) of the raw data variance than multilinear regression (~39%), and a global monthly climatology of sea  
88 surface DMS concentration has been developed based on ANN model (Wang et al., 2020). The machine learning techniques  
89 have also been used to simulate the distribution of DMS in the Arctic (Humphries et al., 2012; Qu et al., 2016), North Atlantic  
90 Ocean (Bell et al., 2021; Mansour et al., 2023), Northeast Pacific Ocean (McNabb and Tortell, 2022), Southern Ocean  
91 (McNabb and Tortell, 2023), and East Asia (Zhao et al., 2022).

92 However, to our best knowledge, there is currently no global-scale sea surface gridded DMS dataset with both high time  
93 resolution (daily) and long-term coverage (> 10 years). Such a dataset is urgently needed for modeling the atmospheric  
94 processes and climatic implications of oceanic DMS. The sea surface concentration and sea-to-air emission flux of DMS can  
95 vary greatly from day to day (Simó and Pedrós-Alió, 1999b), and the emitted DMS exerts effects on the atmosphere over time  
96 scales of several hours to days. Relying solely on monthly climatology of DMS as the emission inventory may fail to capture  
97 important details and could lead to large modeling biases compared to observed concentrations of atmospheric DMS or its  
98 oxidation products (Chen et al., 2018; Fung et al., 2022).

99 Here, we build a 20-year (1998 – 2017) global sea surface DMS gridded dataset ( $1^\circ \times 1^\circ$ ) with a daily resolution based on a  
100 data-driven machine learning approach (ANN ensemble). This product can improve our understanding of the spatiotemporal  
101 variations of oceanic DMS. More importantly, it can serve as an updated emission inventory of marine biogenic DMS for  
102 chemical transport models, which is beneficial for enhancing the simulation of atmospheric processes of DMS and reducing  
103 the uncertainties in marine aerosol's climate effects. The paper consists of four main parts as depicted in Fig. 1: (1) the  
104 development of machine learning model based on global DMS measurements and 9 ancillary environmental variables; (2) the  
105 derived spatial and temporal distributions of DMS and comparisons with previous estimates; (3) an example showing the  
106 superiority of our newly developed DMS field through its correlation with atmospheric biogenic sulfur; and (4) the  
107 uncertainties and limitations inherent in our approach and the resulting data product.





109  
110 **Figure 1.** Flowchart of this study, including the development of ANN ensemble model, construction of new DMS gridded  
111 dataset, and subsequent evaluations of this product.

112 **2 Methodology**

113 **2.1 Input datasets**

114 The in-situ DMS measurement data used for training the machine learning model primarily sourced from the Global Surface  
115 Seawater DMS (GSSD) database (Kettle et al., 1999). The GSSD database contains a total of 87,801 DMS measurements  
116 collected across 266 cruise and fixed-site observation campaigns from 11 March 1972 to 27 August 2017  
117 (<https://saga.pmel.noaa.gov/dms/>, last access: 1 April 2020). Hulswar et al. (2022) consolidated other DMS measurements not  
118 included in the GSSD database to establish an updated DMS climatology. Here we incorporated these additional data predating  
119 2017, originating from 8 campaigns (number of samples = 6,711). The spatial distribution of these combined 94,512 in-situ  
120 observational data is shown in Fig. S1, which covers all major regions of the global ocean.

121 We selected 9 environmental variables relevant to DMS biogeochemical processes as input features, including chlorophyll *a*  
122 (Chl *a*), sea surface temperature (SST), mixed layer depth (MLD), nitrate, phosphate, silicate, dissolved oxygen (DO),  
123 downward short-wave radiation flux (DSWF), and sea surface salinity (SSS). The data sources and relevant information of  
124 these 9 input variables and DMS are listed in Table 1. Chl *a* data were obtained from both in-situ observations, co-located with  
125 DMS data, and satellite remote sensing products (Copernicus-GlobColour, Level-4, daily,  $0.042^\circ \times 0.042^\circ$ ). The Copernicus-  
126 GlobColour Level-4 dataset integrates multiple upstream sensors including SeaWiFS, MODIS-Aqua & Terra, MERIS, VIIRS-  
127 SNPP & JPSS1, and OLCI-S3A & S3B, with an interpolation procedure applied to fill missing data (Garnesson et al., 2019).  
128 Daily SST data ( $0.25^\circ \times 0.25^\circ$ ) were from the NOAA OI SST V2 high-resolution blended reanalysis dataset (Huang et al.,  
129 2021). Daily MLD, DSWF, and SSS were from the modeling outputs of NASA's "Estimating the Circulation and Climate of  
130 the Ocean" (ECCO) consortium, Version 4 Release 4 (V4r4) (Forget et al., 2015). The sea surface concentrations of nitrate,  
131 phosphate, silicate, and DO were from the CMEMS global biogeochemical multi-year hindcast dataset (daily,  $0.25^\circ \times 0.25^\circ$ ).  
132 The surface wind speed (WS) and sea ice fraction (SI) data are needed in the calculation of sea-to-air flux (details are provided  
133 in Section 2.4.2). Here we utilized the daily 10-meter WS data from ECCO V4r4 and the daily SI data from NOAA OI SST  
134 V2. Since there are multiple different spatial grids among all datasets, the data match-up has been conducted as described in  
135 the next section.

136

137 **Table 1.** The data sources and related\_relevant information of variables used for model development, DMS simulation, and  
 138 flux calculation

Variable	Data source	URL	Temporal resolution	Temporal coverage	Spatial grid
DMS	GSSD database	<a href="https://saga.pmel.noaa.gov/dms/">https://saga.pmel.noaa.gov/dms/</a>	In-situ	Mar. 1972 – Aug. 2017	-
	Other campaigns integrated in Hulswar et al. (2022)	<a href="https://data.mendeley.com/datasets/hyn62spny2/1">https://data.mendeley.com/datasets/hyn62spny2/1</a>	In-situ	Feb. 2000 – Jun. 2016	-
Chl <i>a</i>	GSSD database	<a href="https://saga.pmel.noaa.gov/dms/">https://saga.pmel.noaa.gov/dms/</a>	In-situ	Oct. 1980 – Aug. 2017	-
	Copernicus-GlobColour Level-4	<a href="https://data.marine.copernicus.eu/product/OCEANC_OLOUR_GLO_BGC_L4_MY_009_104/description">https://data.marine.copernicus.eu/product/OCEANC_OLOUR_GLO_BGC_L4_MY_009_104/description</a>	Daily	Sep. 1997 – present	0.042°×0.042°
CMEMS	CMEMS global biogeochemical multi-year hindcast (only used for the simulation of DMS concentration in polar regions when satellite Chl <i>a</i> is unavailable)	<a href="https://data.marine.copernicus.eu/product/GLOBAL_MULTIYEAR_BGC_001_029/description">https://data.marine.copernicus.eu/product/GLOBAL_MULTIYEAR_BGC_001_029/description</a>	Daily	Jan. 1993 – present	0.25°×0.25°
	SST	<a href="https://psl.noaa.gov/data/gridded/data.noaa.oisst.v2.hi.ghres.html">https://psl.noaa.gov/data/gridded/data.noaa.oisst.v2.hi.ghres.html</a>	Daily	Sep. 1981 – present	0.25°×0.25°
MLD					
DSWF	NASA ECCO V4r4	<a href="https://data.nas.nasa.gov/ecco/data.php?dir=/eccodata/lle_90/ECCOv4/Release4">https://data.nas.nasa.gov/ecco/data.php?dir=/eccodata/lle_90/ECCOv4/Release4</a>	Daily	Jan. 1992 – Dec. 2017	LLC90 (22 – 110 km)
SSS					
Nitrate					
Phosphate	CMEMS global biogeochemical multi-year hindcast	<a href="https://data.marine.copernicus.eu/product/GLOBAL_MULTIYEAR_BGC_001_029/description">https://data.marine.copernicus.eu/product/GLOBAL_MULTIYEAR_BGC_001_029/description</a>	Daily	Jan. 1993 – present	0.25°×0.25°
Silicate					
DO					
WS	NASA ECCO V4r4	<a href="https://data.nas.nasa.gov/ecco/data.php?dir=/eccodata/lle_90/ECCOv4/Release4">https://data.nas.nasa.gov/ecco/data.php?dir=/eccodata/lle_90/ECCOv4/Release4</a>	Daily	Jan. 1992 – Dec. 2017	LLC90 (22 – 110 km)
SI	NOAA OI SST V2	<a href="https://psl.noaa.gov/data/gridded/data.noaa.oisst.v2.hi.ghres.html">https://psl.noaa.gov/data/gridded/data.noaa.oisst.v2.hi.ghres.html</a>	Daily	Sep. 1981 – present	0.25°×0.25°

139

## 140 2.2 Data preprocessing for model development

141 The data extraction and match-up were performed based on the sampling location and time associated with each DMS  
 142 measurement record, as well as the temporal range and grid distribution of each variable. For satellite-retrieved Chl *a*, the data  
 143 of the grids covering DMS sampling locations were extracted. If the data of the corresponding grid is missing, the average

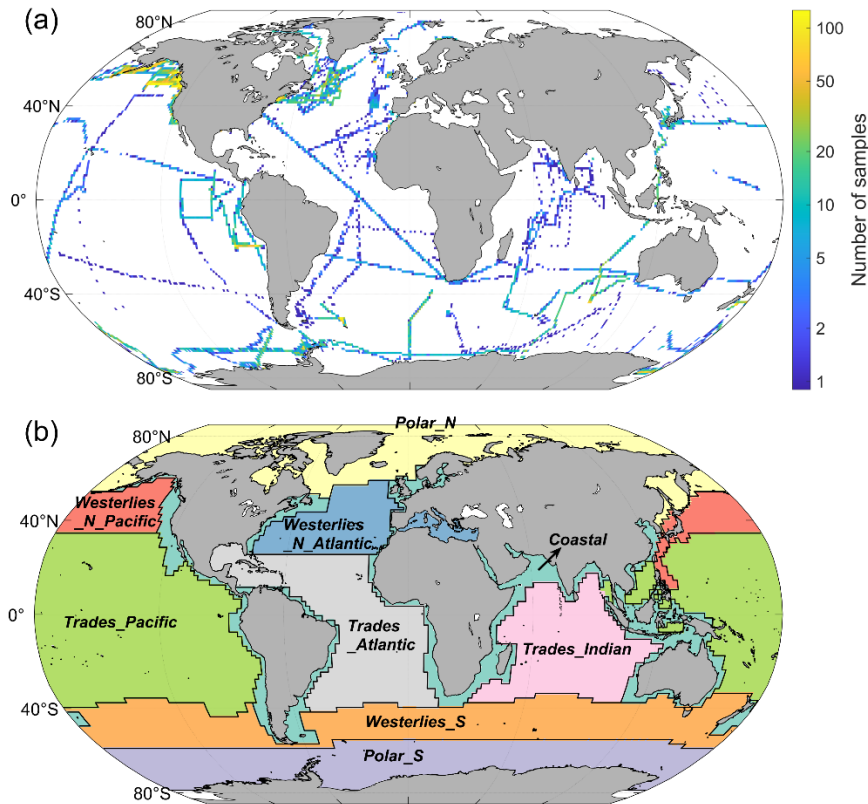
144 value of the  $5 \times 5$  grids nearby was calculated and used. For other variables, only values in the grids matching the DMS sampling  
145 locations were extracted.

146 There are in-situ Chl  $\alpha$  measurements co-located with certain GSSD data. They were also used along with satellite-retrieved  
147 Chl  $\alpha$ . In-situ Chl  $\alpha$  measurements with low precision (defined as  $< 0.1 \text{ mg m}^{-3}$ , and the number of significant digits is 1) were  
148 removed. For a specific in-situ observation campaign, if the number of low-precision values is larger than 10 and accounts for  
149 more than half, all in-situ Chl  $\alpha$  data from this campaign were excluded. In addition, the in-situ Chl  $\alpha$  data in the GSSD database  
150 were measured by two different methods: Turner fluorometry and high-performance liquid chromatography (HPLC). In order  
151 to improve mutual consistency, a conversion between the data from these two methods was applied and then the in-situ Chl  $\alpha$   
152 concentrations were adjusted to match up with satellite Chl  $\alpha$  following the functions described in Galí et al. (2015). After that,  
153 the statistical outliers for all  $\log_{10}(\text{Chl } \alpha)$  (outside the range of average  $\pm 3$  standard deviations) were eliminated. The  
154 comparison between in-situ and satellite-retrieved Chl  $\alpha$  data is shown in Fig. S2. A strong consistency between in-situ and  
155 daily satellite Chl  $\alpha$  data ( $R^2 > 0.5$ , RMSE  $< 0.4$ ) suggests the rationale for integrating these datasets. The  $\log_{10}$  transformation  
156 was applied to make the data distribution close to normal distribution. When finally selecting the  $\log_{10}(\text{Chl } \alpha)$  corresponding  
157 to each DMS data, in-situ data were prioritized where available; otherwise, the satellite-retrieved data were used.

158 DMS and extracted MLD and three nutrients (nitrate, phosphate, silicate) were also performed  $\log_{10}$  transformation. The  
159 statistical outliers of each variable were excluded as mentioned above. After data filtration, a total of 633,361 samples with  
160 valid data for all variables were obtained. To avoid data aggregation bias stemming from multiple data points gathered within  
161 a narrow temporal and spatial range (i.e., the same day and within a region smaller than  $0.05^\circ \times 0.05^\circ$ ), these data points were  
162 averaged. Consequently, 41,157 binned samples were utilized for subsequent model development, with their spatial  
163 distribution depicted in Fig. 2a.

164 We divided the global ocean into 9 regions based on Longhurst's biomes (Longhurst, 1998). There are 6 biomes in  
165 Longhurst's definition, including Coastal, Polar\_N, Polar\_S, Westerlies\_N, Westerlies\_S, and Trades (the .shp file of  
166 Longhurst's biomes and provinces was downloaded from <https://www.marineregions.org/downloads.php#longhurst>). We  
167 further divided Westerlies\_N into Westerlies\_N\_Pacific and Westerlies\_N\_Atlantic, and divided Trades into Trades\_Pacific,  
168 Trades\_Indian, and Trades\_Atlantic by different oceanic basins, as shown in Fig. 2b. It is noteworthy that there are 11,237  
169 samples in the Coastal region, constituting 27.3% of the entire sample set, despite the Coastal biome accounting for only  
170 9.7% of the global ocean area. Given the distinct seawater physiochemical and biological conditions in coastal seas  
171 compared to other regions, the disproportionately higher density of samples within the Coastal biome might cause the model  
172 to overly prioritize this region. To mitigate this data imbalance and ensure the model captures broader patterns in open  
173 oceans, we adjusted the data distribution during model training and validation processes. Specifically, for each training  
174 session, a portion of coastal samples is randomly removed, ensuring the proportion of coastal samples in the total sample set

175 (denoted as  $F_{\text{coastal}}$ ) matches its area proportion, we adjusted the fraction of coastal samples to match the area fraction. Further  
176 details are provided in the subsequent section and visualized in Fig. 3a.



177  
178 **Figure 2.** (a) The distribution of 41,157 DMS observational data after matchup, filtration, and binning for constructing the  
179 ANN model. The grid size is  $1^\circ \times 1^\circ$ . (b) Nine oceanic regions separated based on Longhurst's biomes (Longhurst, 1998).  
180

### 181 2.3 Artificial neural network training and validation

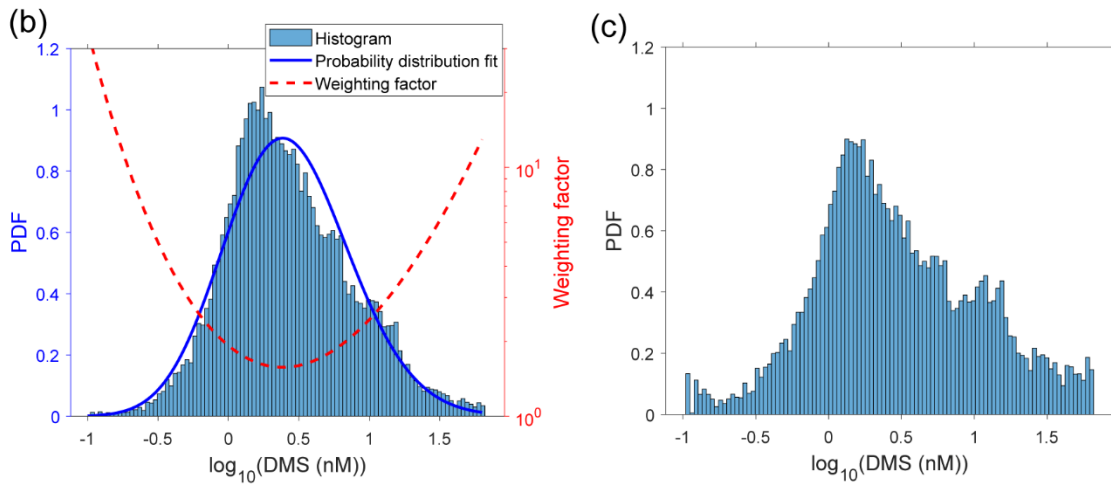
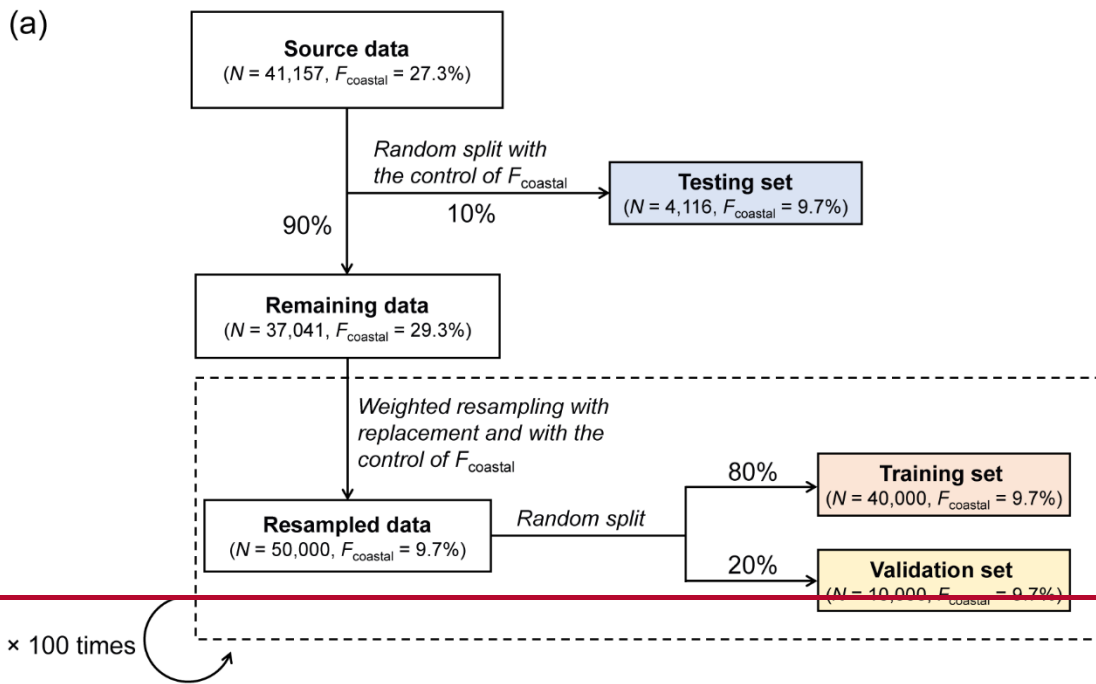
182 The 41,157 binned samples after the previously mentioned data preprocessing were used to develop the artificial neural  
183 network (ANN) model. The target feature is  $\log_{10}(\text{DMS})$ , and the input features are  $\log_{10}(\text{Chl } a)$ , SST,  $\log_{10}(\text{MLD})$ ,  
184  $\log_{10}(\text{nitrate})$ ,  $\log_{10}(\text{phosphate})$ ,  $\log_{10}(\text{silicate})$ , DO, DSWF, and SSS. The data of all variables were standardized before  
185 training.

186 We randomly selected 10% of the samples ( $n = 4,116$ ) to be entirely excluded from training, as a testing subset for global  
187 validation and overfitting test. The testing subset was controlled to contain a proportion of coastal samples (denoted as  $F_{\text{coastal}}$ )  
188 at 9.7%. Specifically, 401 samples were randomly selected from Coastal biome, and while 3,715 samples were selected from

189 other biomes to compose the testing subset, matching the proportion of coastal area in global oceans (9.7%). Then, the  
190 remaining samples ( $n = 37,041$ ) were utilized for training and cross validation, with a constraint of  $F_{\text{coastal}}$  equal to 9.7% in  
191 each training session as mentioned above. Apart from the data imbalance between coastal and non-coastal regions, there exists  
192 an imbalance across different DMS concentration ranges. As shown in Fig. 3b, the majority of DMS concentration values  
193 (78.6%) fall within the range of 0.8 to 10 nM ( $\log_{10}(\text{DMS})$  between 0.1 to 1). Samples with DMS concentrations exceeding  
194 15 nM or falling below 0.3 nM only represent 6.9% of the entire sample set. Here we implemented a weighted resampling  
195 strategy to mitigate this imbalance and enhance the model's capability in predicting extreme values. We randomly sampled  
196 50,000 samples with replacement from the remaining sample set. The probability of each sample being selected is proportional  
197 to the weighting factor shown in Fig. 3b, which is dependent on its DMS concentration. Samples exhibiting high or low DMS  
198 concentration values are more likely to be selected, whereas those with intermediate concentrations are less likely to be  
199 selected. The details of the weighting factor are explained in Appendix B. We also controlled the  $F_{\text{coastal}}$  value of the resampled  
200 data equals to 9.7% by the same method as described above, i.e., applying the resampling process to coastal and non-coastal  
201 samples separately and combining them together afterwards. The data distribution of DMS concentrations after the resampling  
202 process is shown in Fig. 3c. The fraction of samples with DMS concentrations above 15 nM or below 0.3 nM is elevated to  
203 15.0%. The 50,000 samples were then randomly split to a training set (80%) and a validation set (20%). Since there are  
204 duplicate samples in the resampled dataset, the random data split was conducted based on the original sample ID before  
205 resampling to ensure that there was no sample overlap between the training and validation sets.

206 Our feedforward fully connected neural network comprises two hidden layers, with 15 nodes in each layer. The activation  
207 functions for the first and second layers are ReLU and tanh, respectively. We applied L2 regularization ( $\text{lambda} = 5\text{E}1\text{E}-4$ ) to  
208 counteract overfitting. The loss function is mean square error (MSE). Training stops if the validation loss is greater than or  
209 equal to the minimum validation loss computed so far 20 times in a row. The training processes were carried out with Statistics  
210 and Machine Learning Toolbox on Matlab 2022b. We repeated the data resampling, split, (for training and validation sets)  
211 and training processes for 100 times and obtained 100 neural networks. The average prediction results of multiple ANNs shows  
212 a much higher consistency with the observations than a single ANN (Fig. S3). As the number of ANNs ( $N_{\text{training}}$ ) increases, the  
213 accuracy of model predictions initially improves and then diminishes, eventually stabilizing/stabilizes. We adopted the average  
214 output of 10-20 ANNs as the final output, balancing performance and computational costs effectively. This kind of multiple-  
215 training approach, often termed “ANN ensemble” or “Monte Carlo cross-validation”, has been widely used to improve the  
216 model generalization and performance (Sigmund et al., 2020; Holder et al., 2022) as well as get a better model evaluation  
217 (Dubitzky et al., 2007).

218



219

220 **Figure 3.** Data split and resampling strategy for ANN model training and testing. (a) Flowchart of the data split and resampling  
 221 procedures.  $N$  and  $F_{\text{coastal}}$  denote the number of samples and the fraction of coastal samples, respectively. (b) The probability  
 222 distribution of raw  $\log_{10}(\text{DMS})$  values and the relationship between the weighting factor for weighted resampling and  
 223  $\log_{10}(\text{DMS})$  value. PDF represents the probability density function. (c) The probability distribution of  $\log_{10}(\text{DMS})$  values after  
 224 weighted resampling.

225 **2.4 Deriving the 20-year global DMS distributions**226 **2.4.1 Simulation of sea surface DMS concentrations**

227 First, we constructed the daily gridded dataset of input variables with a spatial resolution of  $1^\circ \times 1^\circ$  from 1998 to 2017 ~~using~~  
 228 based on the data sources listed in Table 1 (except in-situ Chl *a* data). Datasets with a higher spatial resolution than  $1^\circ \times 1^\circ$  were  
 229 binned into  $1^\circ \times 1^\circ$ . In polar regions, the satellite Chl *a* data are missing during winter, and the Chl *a* data from CMEMS global  
 230 biogeochemical multi-year hindcast were used to fill the missing values. Then, the obtained gridded dataset was fed into the  
 231 ANN ensemble model, and the 20-year global distribution of sea surface DMS concentration with daily resolution was  
 232 simulated.

233 **2.4.2 Calculation of sea-to-air fluxes**

234 The sea-to-air fluxes of DMS were calculated on the basis of simulated surface DMS concentrations following equation (1):

$$235 DMS \text{ flux} = Kt \times (DMS_w - \frac{DMS_a}{H}) \quad (1)$$

236 Here  $DMS_w$  and  $DMS_a$  are DMS concentrations in surface seawater and air, respectively.  $H$  is Henry's law constant of DMS.  
 237 Since  $\frac{DMS_a}{H}$  is usually  $\ll DMS_w$ , this term was omitted in the calculation.  $Kt$  is the total transfer velocity considering the sea  
 238 ice coverage fraction (*SI*):

$$239 Kt = k_t \times (1 - SI) \quad (2)$$

240  $k_t$  is the total transfer velocity without considering sea ice which is calculated by equation (3):

$$241 \frac{1}{k_t} = \frac{1}{k_w} + \frac{1}{k_a \times H} \quad (3)$$

242 Here  $k_w$  and  $k_a$  are the water-side transfer velocity and air-side transfer velocity, respectively. We used the same approach as  
 243 Galí et al. (2019) to obtain  $k_w$ ,  $k_a$ , and  $H$  for DMS, where the effect of wind speed was considered for  $k_a$ , and the influences of  
 244 SST and SSS were considered for  $H$ . The calculations of  $k_a$  and  $H$  followed the parameterizations of Johnson (2010). As for  
 245  $k_w$  calculation, we adopted the bubble scheme (Woolf, 1997), which divided the sea-to-air mass transfer process into  
 246 turbulence- and bubble-mediated gas exchange. The calculated  $k_w$  based on the bubble scheme is lower than that of  
 247 Nightingale's scheme (Nightingale et al., 2000) under conditions of high wind speed, exhibiting a smaller deviation from the  
 248 ~~actual value measurements~~ (Beale et al., 2014; Galí et al., 2019). Before calculation, WS and SI data were also binned by  $1^\circ \times 1^\circ$   
 249 grid. By using WS and SI together with SST and SSS datasets, we obtained the daily gridded  $Kt$  and then calculated the sea-  
 250 to-air DMS fluxes (daily, 1998–2017) by multiplying simulated DMS concentrations by  $Kt$  values.

251 **3 Results**252 **3.1 Model performance**

253 As shown in Fig. 4a3a, the newly developed ANN ensemble model captures a substantial part of data variance globally ( $\log_{10}$   
 254 space  $R^2 = 0.612\text{--}651$  and RMSE = 0.276262). 91.692.8% of ANN simulated concentration values fall within 1/3 to 3 times of  
 255 corresponding true values. The performance for testing set ( $R^2 = 0.606\text{--}640$ , RMSE = 0.282267, and 90.892.7% of data within  
 256 the range of 1/3 to 3 times of observations) is very close to that for the training dataset (Fig. 4b3b), suggesting no obvious  
 257 overfitting. The ANN model exhibits better performance compared to previous empirical and process-based models ( $R^2 =$   
 258 0.01~0.14) (Tesdal et al., 2016) as well as the satellite-based algorithm ( $R^2 = 0.50$ ) (Gali et al., 2018). The ANN model  
 259 developed by Wang et al. (2020) showed a slightly higher similar performance ( $R^2 = 0.66$ , RMSE = 0.264 for training dataset)  
 260 than to our model, likely due to despite their more complex ANN configuration (two hidden layers with 128 nodes each) and  
 261 the including inclusion of sample location and time into input features. However, the more complex model will significantly  
 262 increase the computational cost, and the incorporation of location and time information may weaken the physical  
 263 interpretability. ~~On the other hand, the performance improvement is very limited. Therefore, we keep the simpler model  
 264 configuration.~~

265 The performance of the model was evaluated across each of the nine oceanic regions. As illustrated in Fig. 4e3c and 4, the  
 266  $\log_{10}$  space RMSEs are all below 0.33~32 (equivalent to a concentration ratio of 2.13~09 in linear space), except for the Coastal  
 267 region (training: RMSE = 0.362~322,  $R^2 = 0.479$ ; testing: RMSE = 0.332,  $R^2 = 0.480$  and  $R^2 = 0.384$ ). Since the Coastal region  
 268 comprises only 9.7% of the global oceanic area, the comparatively lower performance in this area has minimal impact on the  
 269 overall ability to predict the spatiotemporal distributions of DMS on a global scale. Despite the  $R^2$  values in Trades\_Pacific  
 270 and Trades\_Atlantic being lower than 0.5, which is related to the relatively narrow variation range of DMS concentration, the  
 271 RMSEs in these regions remain quite low and comparable to those of other regions. In general, our ANN ensemble model  
 272 demonstrates a satisfactory capacity to reproduce variations in DMS concentrations across diverse oceanic regions.

273 However, it is noteworthy that our model tends to underestimate extremely high DMS concentrations and overestimate  
 274 extremely low concentrations. Overall, the linear regressions between ANN-predicted and observed DMS concentrations yield  
 275 slopes significantly lower than unity across all regions (Fig. 3c and 4), and there are significantly positive correlations between  
 276 prediction residuals (observation – prediction) and observed  $\log_{10}(\text{DMS})$  (Fig. S5 and S6). From a data perspective, this may  
 277 be partly due to the insufficient number of samples with extreme DMS concentrations (known as underrepresentation), making  
 278 it difficult to adequately capture the relevant information during training process. To test this point, we adopted a weighted  
 279 resampling strategy to bolster the number of samples in the minority class before training, which has been widely used in  
 280 machine learning to deal with the data imbalance issue (Haibo et al., 2008; Yu and Zhou, 2021; Chawla et al., 2002). The basic  
 281 idea is to set a higher probability of being sampled for the minority class with extreme DMS concentrations, and the details

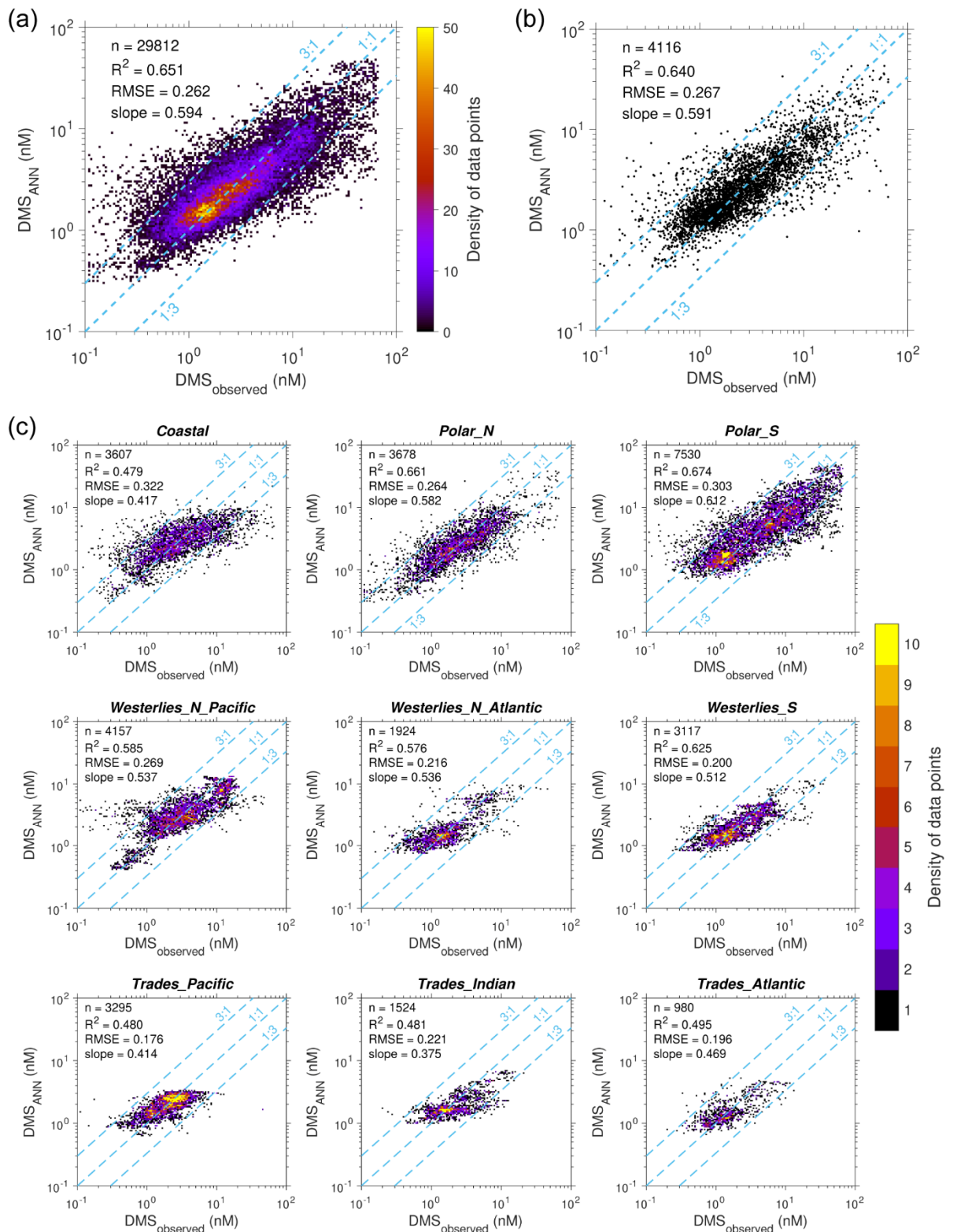
282 are illustrated in Fig. S7 and explained in Appendix B. The results indicate that the weighted resampling scheme cannot fully  
283 alleviate the model bias. Although it does elevate the overall prediction-versus-observation slopes from ~0.59 to ~0.63, this  
284 improvement is marginal (Fig. S8 and S9). In several regions like Westerlies\_S and Trades biomes, the slopes are even lower  
285 than original values. Furthermore, the data become more scattered after implementing the weighted resampling, resulting in  
286 increased RMSE and decreased R<sup>2</sup>. Therefore, there are other potential issues causing the model bias, which are discussed in  
287 Section 4. The original model, trained without weighted resampling, was adopted for subsequent analysis and the construction  
288 of the gridded DMS dataset.

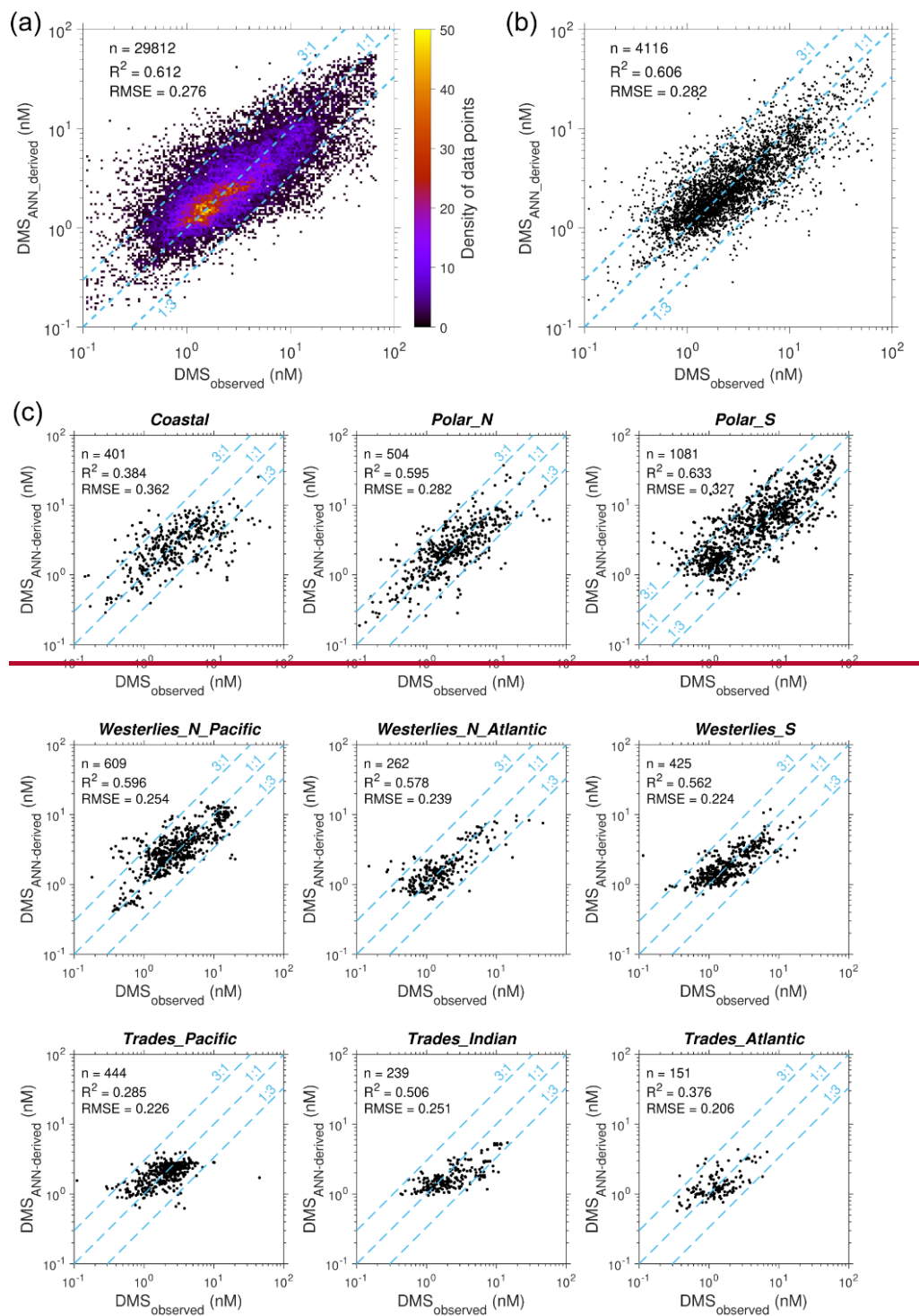
289

290 While we have implemented a weighted resampling strategy to bolster the number of samples with extreme DMS  
291 concentrations prior to training, aiming to enhance the model performance in predicting such extreme values, the model still  
292 tends to underestimate the extremely high DMS concentrations and overestimate the extremely low concentrations (Fig. 4 and  
293 Fig. S4). Consequently, significant positive correlations emerge between prediction residuals (observation – prediction) and  
294 observed  $\log_{10}(\text{DMS})$ , particularly evident in Coastal and Trades regions, where the slopes exceed 0.55 (Fig. 5 and Fig. S6).  
295 Given the scarcity of observational data in these high DMS and low DMS regimes, it is considerable challenge to completely  
296 address this issue without succumbing to overfitting via purely data driven approaches. The data augmentation by weighted  
297 resampling can only partially alleviate this issue. It underscores imperative for acquiring more observational data on sea surface  
298 DMS in future endeavours. Moreover, integrating DMS biogeochemical mechanisms with machine learning techniques may  
299 offer a promising avenue to tackle this challenge.

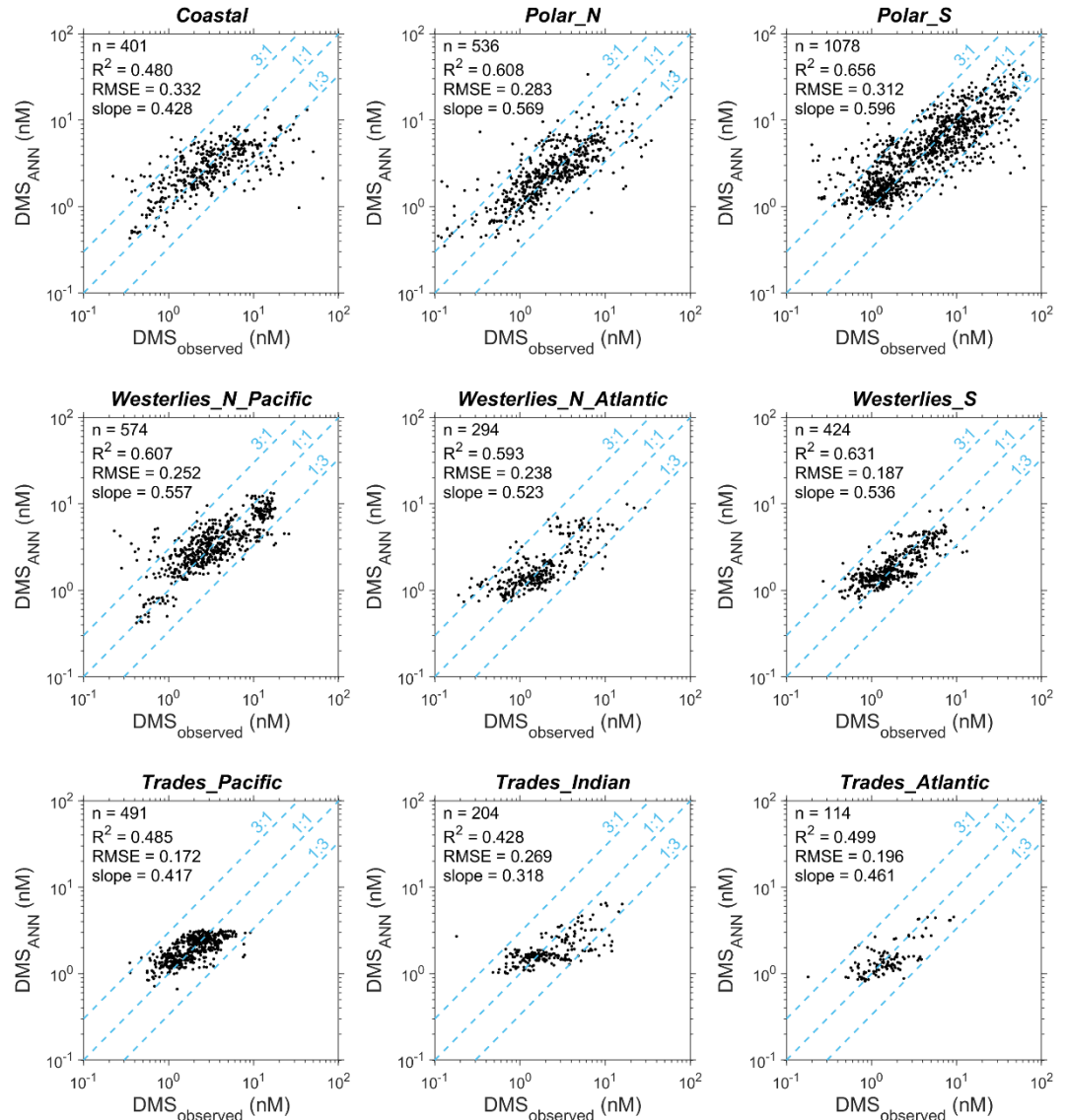
300 Owing Primarily owing to the underestimation of high DMS concentrations, a negative mean bias (MB) in DMS concentration  
301 is evident across all regions, ranging from -0.23\_18 to -1.48\_2.02 nM (Table 2). The normalized mean bias (NMB, the ratio  
302 between mean bias and mean observed concentration) ranges from -11.18\_7% to -32.42%. The most significant NMB emerges  
303 in Coastal and Trades\_India regions, while NMB remains within -2025% for other regions. The global MB and NMB are -  
304 0.771\_05 nM and -16.222\_1%, respectively. It is worth noting that these biases are compared against historical DMS  
305 observations, which were conducted within a very limited geographical area and time periods. Thus, they cannot be interpreted  
306 as the actual mean modelling bias for the entire region. On the other hand, the negative biases at high end of the concentrations  
307 are partially cancelled out by the positive biases at low end during the averaging over the entire region. The bias at a specific  
308 grid could be much larger. Nevertheless, these those extreme DMS concentrations (> 15 nM or < 0.3 nM), exhibiting the most  
309 significant modeling bias, represent only a minority of the entire sample set (6.9%). Our model adeptly reproduces the majority  
310 of observations with moderate DMS concentrations across all regions, with the percentage of simulated predicted values falling  
311 within 1/3 to 3 times of observations ranging from 8887.0% to 99.398.8%.

312





316 **Figure 43.** Comparisons between ANN-simulated and observed DMS concentrations. (a) Scatter density for simulated versus  
 317 observed DMS concentrations of the samples used in ANN training. ~~This plot corresponds to the original data before  
 318 resampling and only a subset of coastal data are included to maintain  $F_{\text{coastal}}$  at 9.7%, which aligns with data composition in  
 319 training.~~ (b) Comparison between the simulated versus observed DMS concentrations of testing set. (c) Comparison between  
 320 the simulated versus observed DMS concentrations of ~~the samples used in ANN training~~ testing set across 9 regions. The  
 321 number of data points (n), ~~the~~  $\log_{10}$  space  $R^2$ , ~~and the~~ root mean square error (RMSE), ~~and~~ linear regression slope are also  
 322 displayed.  
 323

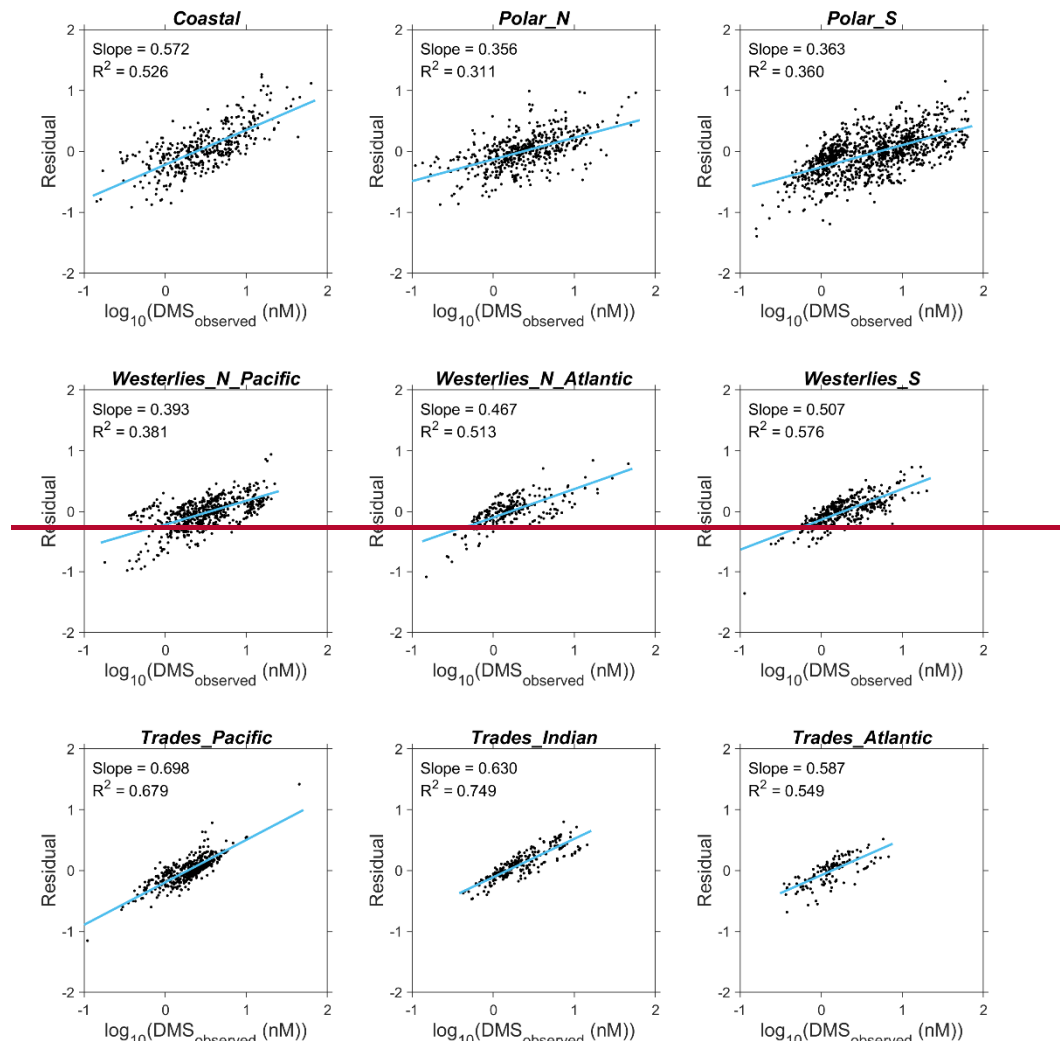


324

325

**Figure 4.** Comparisons between the simulated versus observed DMS concentrations of the testing set across 9 regions.

326



327

**Figure 5.** Correlations between prediction residuals of  $\log_{10}(\text{DMS})$  and observed values across different regions corresponding to the testing set.

330

331 **Table 2.** The mean bias and normalized mean bias of the ANN-predicted DMS concentrations against observations across  
 332 different regions.

Region	Mean bias (nM)	Normalized mean bias
Coastal	-1.48	-29.6%
Polar_N	-0.62	-14.9%

<u>Polar_S</u>	<u>-1.09</u>	<u>-13.0%</u>
<u>Westerlies_N_Pacific</u>	<u>-0.74</u>	<u>-15.3%</u>
<u>Westerlies_N_Atlantic</u>	<u>-0.25</u>	<u>-11.1%</u>
<u>Westerlies_S</u>	<u>-0.44</u>	<u>-17.1%</u>
<u>Trades_Pacific</u>	<u>-0.23</u>	<u>-10.3%</u>
<u>Trades_Indian</u>	<u>-0.88</u>	<u>-32.1%</u>
<u>Trades_Atlantic</u>	<u>-0.24</u>	<u>-13.6%</u>
<u>Global</u>	<u>-0.77</u>	<u>-16.2%</u>

333

Region	Mean bias (nM)	Normalized mean bias
<u>Coastal</u>	<u>-1.55</u>	<u>-32.2%</u>
<u>Polar_N</u>	<u>-0.90</u>	<u>-21.4%</u>
<u>Polar_S</u>	<u>-2.02</u>	<u>-24.1%</u>
<u>Westerlies_N_Pacific</u>	<u>-0.91</u>	<u>-18.8%</u>
<u>Westerlies_N_Atlantic</u>	<u>-0.24</u>	<u>-10.4%</u>
<u>Westerlies_S</u>	<u>-0.36</u>	<u>-14.1%</u>
<u>Trades_Pacific</u>	<u>-0.19</u>	<u>-8.7%</u>
<u>Trades_Indian</u>	<u>-0.73</u>	<u>-26.7%</u>
<u>Trades_Atlantic</u>	<u>-0.18</u>	<u>-10.1%</u>
<u>Global</u>	<u>-1.05</u>	<u>-22.1%</u>

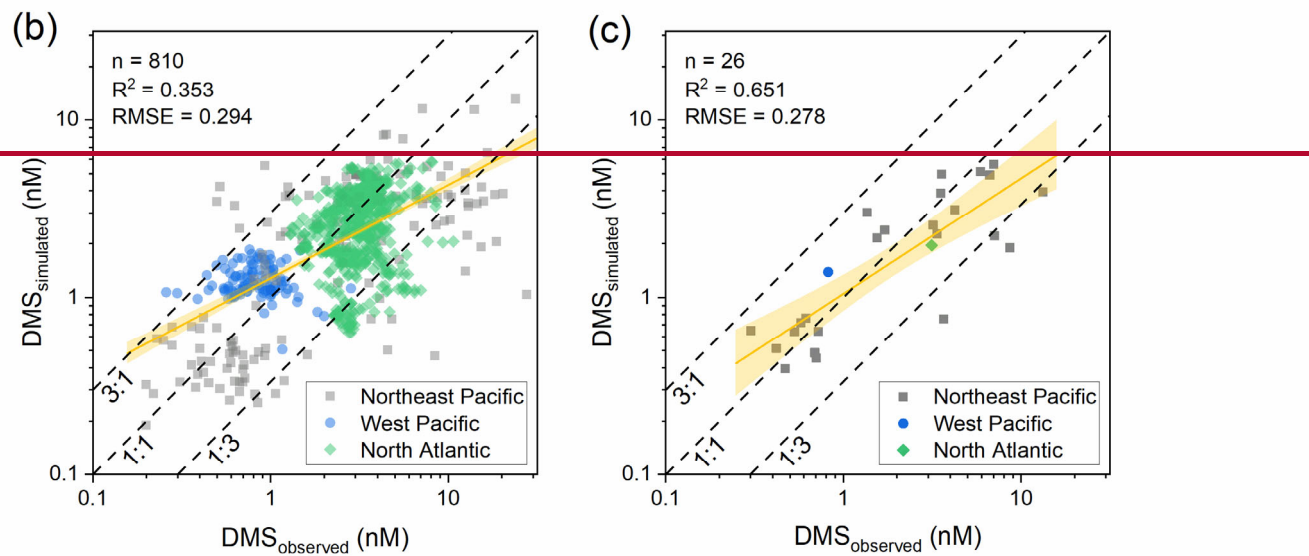
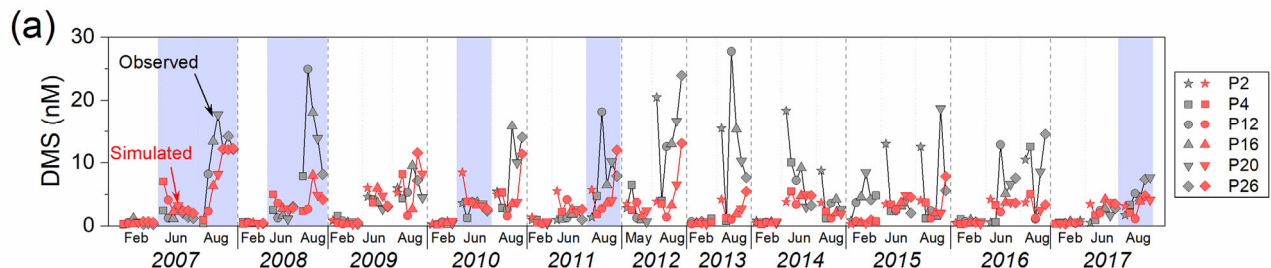
334

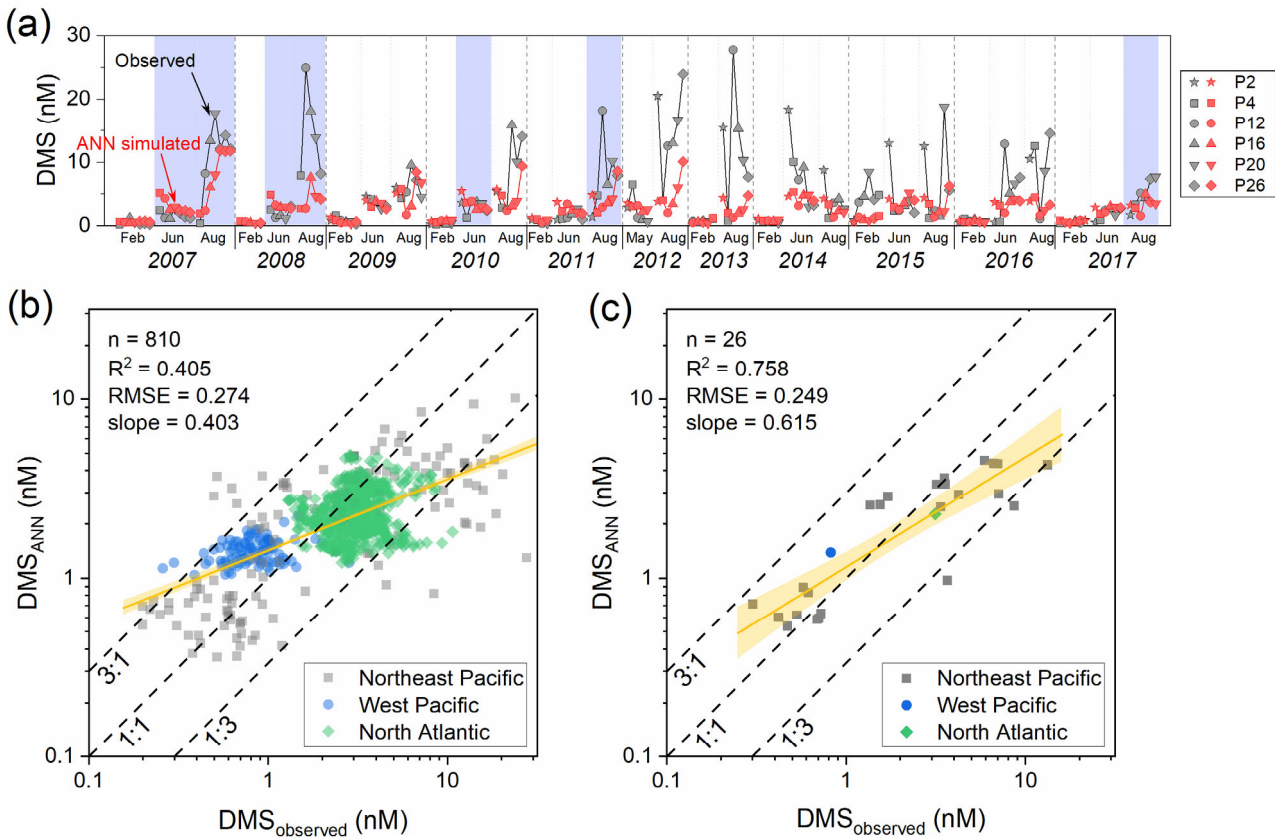
335

336 It is worth noting that there may be intrinsic connections between the 10% excluded testing subset and the training set, because  
 337 the data from the same cruise or fixed-site campaign have certain continuity. To further evaluate the reliability of the ANN  
 338 model, we compared the simulated DMS concentrations with the observational data from fully independent campaigns, which  
 339 are obtained from 33 cruises in Northeast Pacific, West Pacific, and North Atlantic (number of data = 6,478). These data  
 340 include (1) discrete sampling and measurement during 31 cruises of *Line P Program* in Northeast Pacific (Steiner et al., 2011)  
 341 (9 February 2007 – 26 August 2017, number of data = 177, <https://www.waterproperties.ca/linep/index.php>, last access: 23  
 342 November 2020), (2) underway measurements during *SONNE cruise 202/2 (TRANSBROM)* in West Pacific (Zindler et al.,  
 343 2013) (9 – 23 October 2009, number of data = 115, <https://doi.org/10.1594/PANGAEA.805613>, last access: 23 November  
 344 2020), (3) underway measurements during the third *North Atlantic Aerosols and Marine Ecosystems Study (NAAMES)*  
 345 campaign (Behrenfeld et al., 2019; Bell et al., 2021) (6 – 24 September 2017, number of data = 1,025,  
 346 <https://seabass.gsfc.nasa.gov/naames>, last access: 27 November, 2020). Before the comparison, the data measured within a  
 347  $0.05^\circ \times 0.05^\circ$  grid and at the same day were binned by arithmetic average.

348 The comparisons between these observed DMS concentrations and ANN simulation are shown in Fig. 65. Regarding the *Line*  
349 *P Program*, it should be noted that there are 7 cruises included in the GSSD database, but those data were obtained by underway  
350 measurements, different from the discrete sampling (Niskin bottle) data used here. Hence, these cruises were retained and  
351 marked in Fig. 6a-5a but excluded in subsequent statistical analysis (Fig. 6b-5b-c). It can be seen that the model effectively  
352 captures the seasonal variation in Northeast Pacific, which is generally August > June > February (Fig. 6a-5a). However, the  
353 small-scale spatial variations can only be partially reproduced by the model in certain campaigns, such as those in June and  
354 August of 2007, June of 2009, August of 2012, and August of 2016. Notably, the model generally underestimates high DMS  
355 concentrations during summer, particularly those exceeding 10 nM, consistent with earlier discussions. Aggregating data from  
356 all campaigns across three regions, the  $\log_{10}$  space RMSE of simulated DMS concentrations against observations is 0.294274,  
357 marginally higher than the training set. Most simulated values (87.893.0%) are within the range of 1/3 to 3 times of  
358 observations. The results further evidence that there is no significant overfitting in our model. When data from each campaign  
359 are binned, simulations demonstrate high consistency with observations, as depicted in Fig. 6e-5c (RMSE = 0.278249,  $R^2$  =  
360 0.651758). In summary, although our ANN ensemble model may not precisely reproduce small-scale variations and extreme  
361 values in specific regions and periods, it reasonably captures overall large-scale variations.

362





364

365 **Figure 65.** Comparisons between the ANN predictions and observations ~~from~~ ~~for~~ fully independent campaigns. (a) Time series  
 366 of simulation results and DMS observational data obtained from *Line P Program*. The different markers represent different  
 367 stations of *Line P*. The blue shades cover the data obtained from the cruises included in the GSSD database but with a different  
 368 method. (b) Scatter plot of simulated versus observed DMS concentrations. (c) The same as panel b but for averaged data of  
 369 each cruise. The yellow lines and shaded bands are linear fittings and corresponding 95% confidence intervals for  $\log_{10}$  space  
 370 data. The values of  $R^2$ , and RMSE, and slope displayed in the figure also correspond to  $\log_{10}$  space data.

371 

### 3.2 DMS distribution

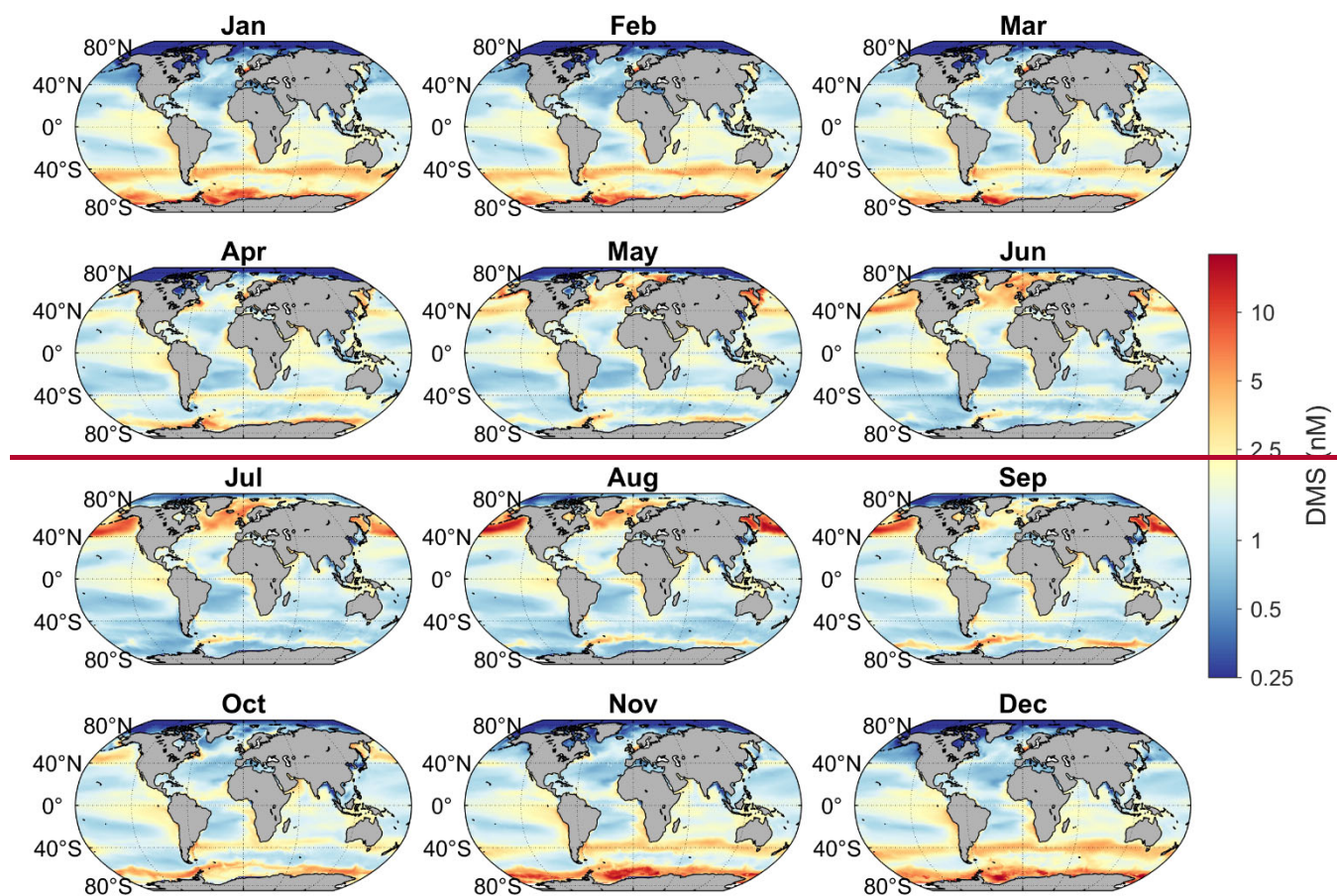
372 

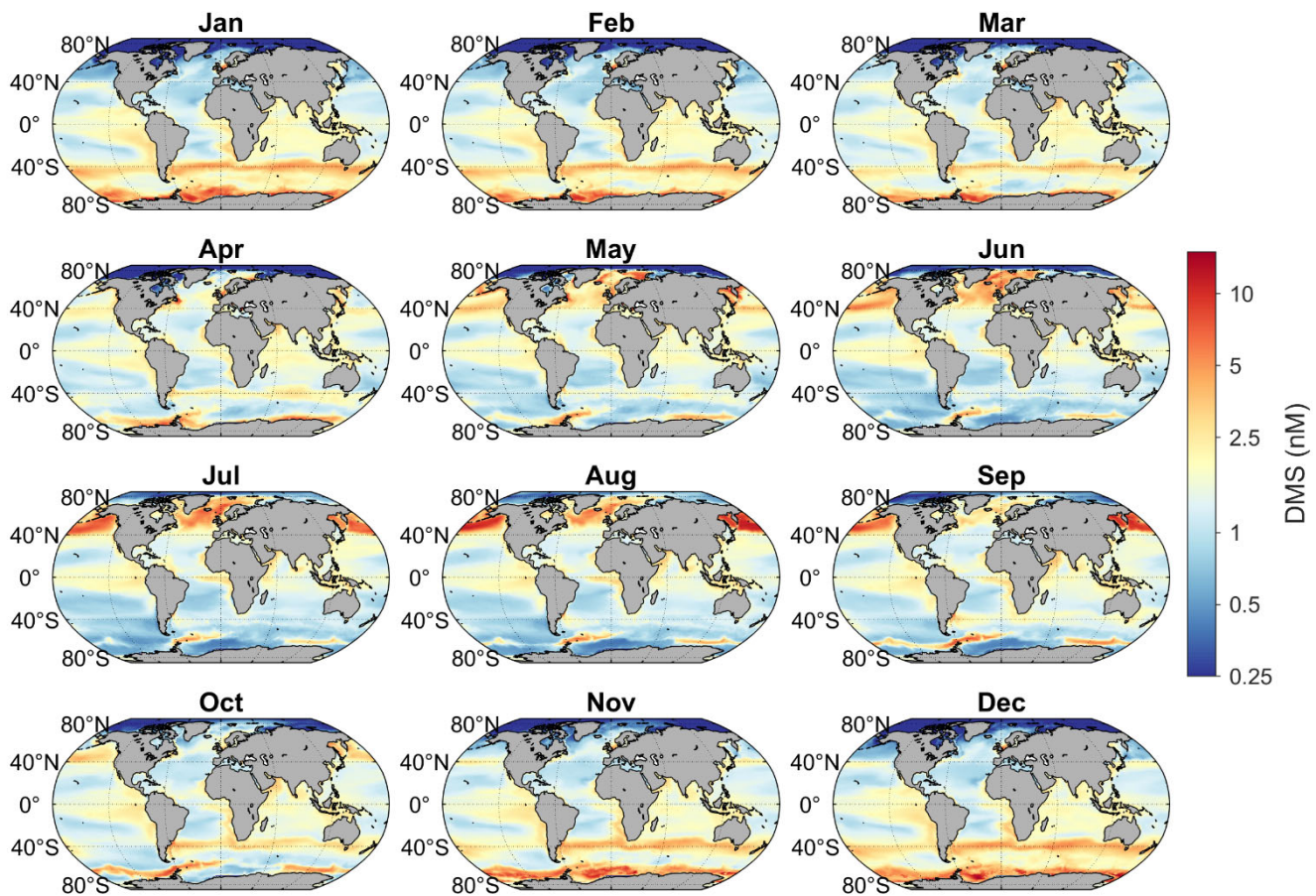
#### 3.2.1 Spatial and seasonal variations

373 The monthly climatology of ANN-simulated DMS concentrations in the global sea surface from 1998 to 2017 is shown in Fig.  
 374 ~~76~~. Overall, the DMS concentrations in mid- and high-latitude regions exhibit a significant seasonal cycle, peaking in summer  
 375 and reaching their lowest in winter. This pattern aligns with the results of many prior observational studies. In the northern  
 376 hemisphere, elevated DMS concentrations ( $> 2.5$  nM) during summer mainly occur in two regions. One is the North Pacific

377 (40°–60° N) where the concentration generally peaks in August, surpassing 10 nM (Fig. 76). The other is the subarctic North  
378 Atlantic (45°–80° N). A notable increase of DMS concentration starts around 45°–50° N in May and gradually shifts northward  
379 beyond 50° N by July (Fig. 76–87). This spatiotemporal evolution pattern corresponds to the evolution of solar radiation  
380 intensity and the spring-summer bloom patterns of phytoplankton (Friedland et al., 2018; Yang et al., 2020). The peak  
381 concentration date at the same latitude in the North Atlantic generally precedes that in the North Pacific (Fig. 87). In the  
382 southern hemisphere, there is a conspicuous DMS-rich zone near 40° S (where the Subtropical Convergence lies) in summer,  
383 delineating a ring-shaped high-concentration band nearly parallel to the latitude. The highest seasonal mean concentration  
384 (December–February) occurs at 4241.5° S, reaching 4.023.71 nM (Fig. 409). Southward from this zone, a low-DMS area spans  
385 4947°–5961° S, where the average concentration is below 2.5 nM across all seasons. However, in the coastal waters of  
386 Antarctica (south of 60° S), significantly high concentrations also manifest in summer, surpassing 54.0 nM, even higher than  
387 those near 40° S (Fig. 76 and 409). In addition to the above regions, several typical upwelling zones also exhibit relatively  
388 higher DMS concentrations, such as the eastern Pacific and the Southeast Atlantic. The former, situated at lower latitudes,  
389 shows no ~~distinct~~significant seasonal variation, while the latter exhibits higher concentrations from October to February. The  
390 high nutrient concentrations in upwelling areas can bolster primary productivity, intensifying biological activities and  
391 augmenting the production of biogenic sulfur.

392

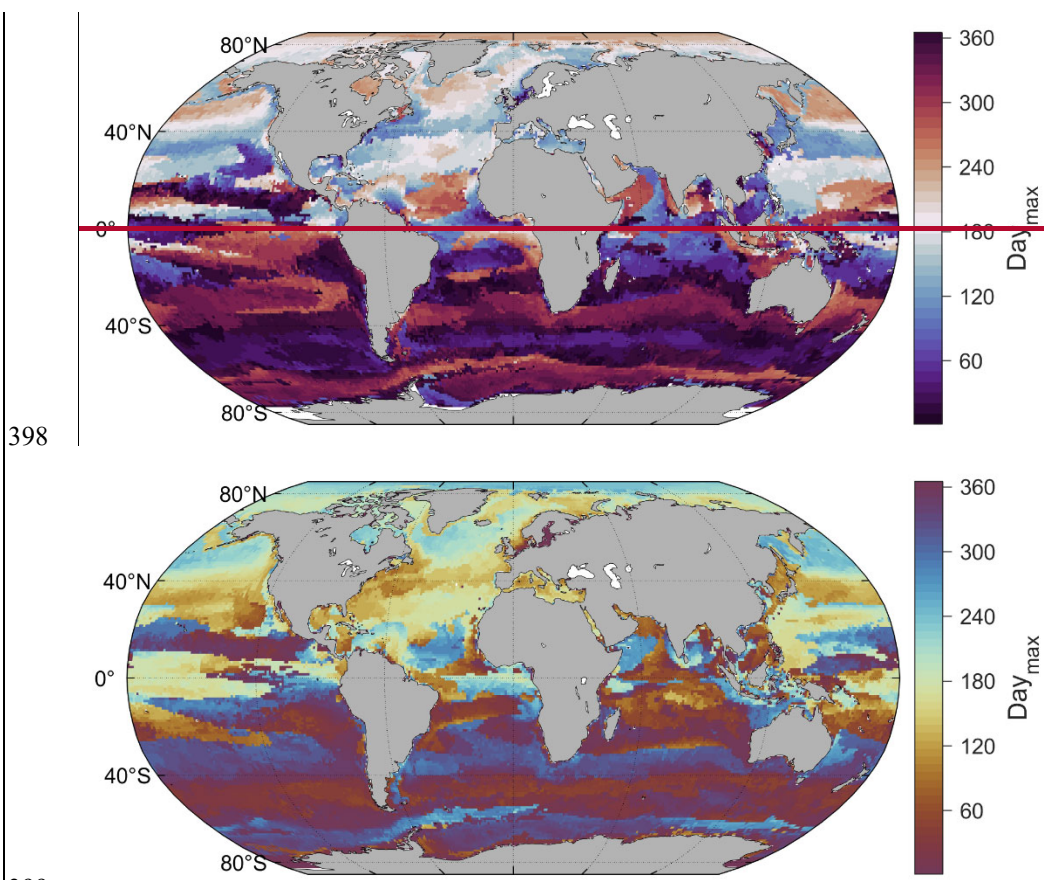




395

396 **Figure 76.** Monthly climatology of global sea surface DMS concentration during 1998 to 2017.

397



400 **Figure 87.** The day of the year with the highest sea surface DMS concentration for each grid point.

401

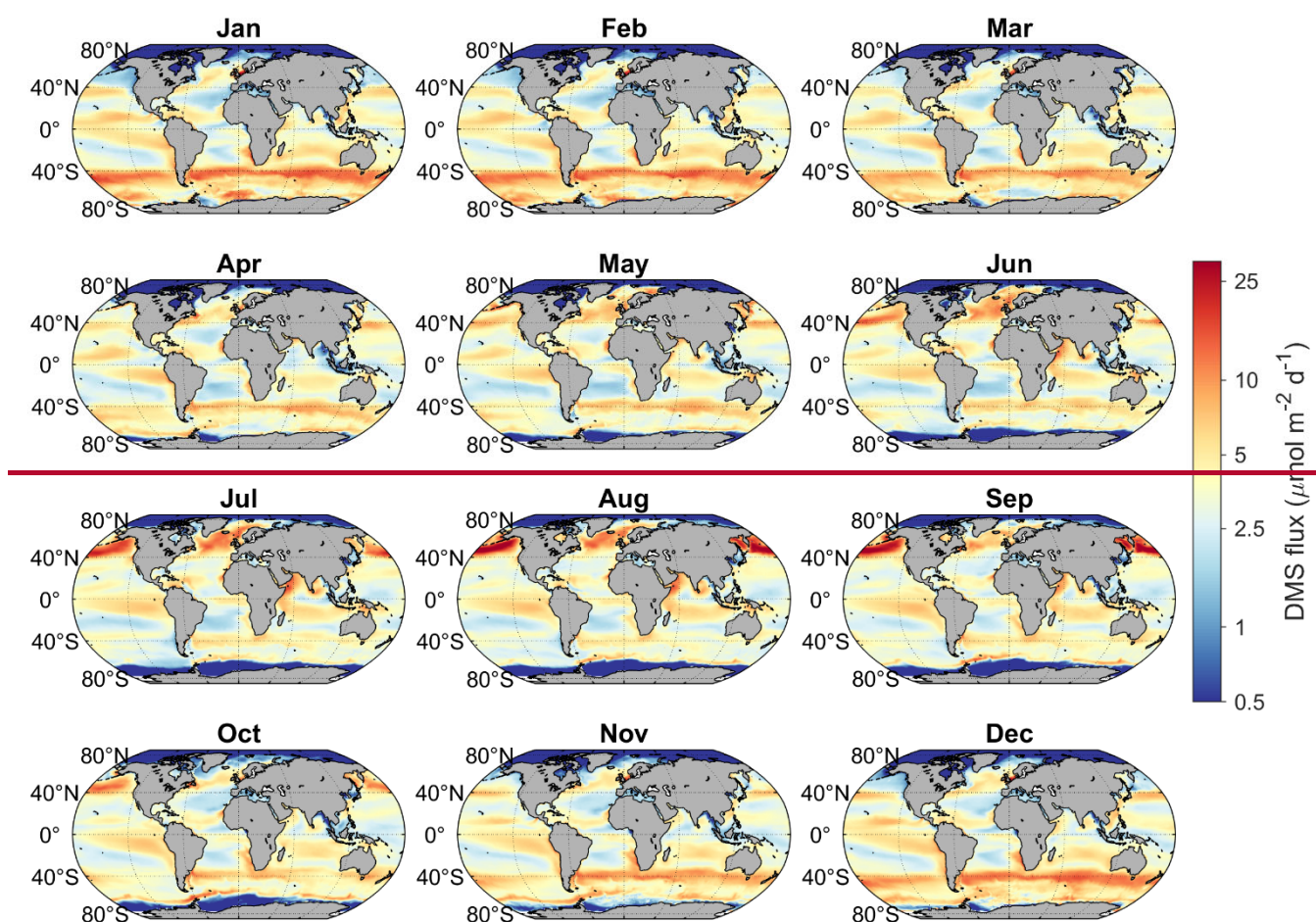
402 The spatiotemporal variation of DMS emission flux is generally consistent with that of concentration. As shown in Fig. 98,  
 403 DMS fluxes are also significantly higher in summer across most mid- and high-latitude regions, and the high-flux regions  
 404 generally overlap with the hot spots of DMS concentration. This indicates that the distribution of sea surface DMS  
 405 concentration is the main factor controlling the monthly variation pattern of DMS emissions at the global scale, and the effect  
 406 of transfer velocity is secondary. However, certain regions present inconsistencies between DMS flux and concentration  
 407 dynamics. For instance, in the Arabian Sea and the central Indian Ocean, elevated transfer velocities (Fig. S7S10) during the  
 408 June to September, driven by heightened wind speeds, markedly enhance emission fluxes, despite comparatively lower  
 409 concentrations than other months. In polar regions, especially along the coast of Antarctica, although the DMS concentration  
 410 is high in summer, sea ice coverage significantly impedes DMS release, thus the emission flux remains at a low level.

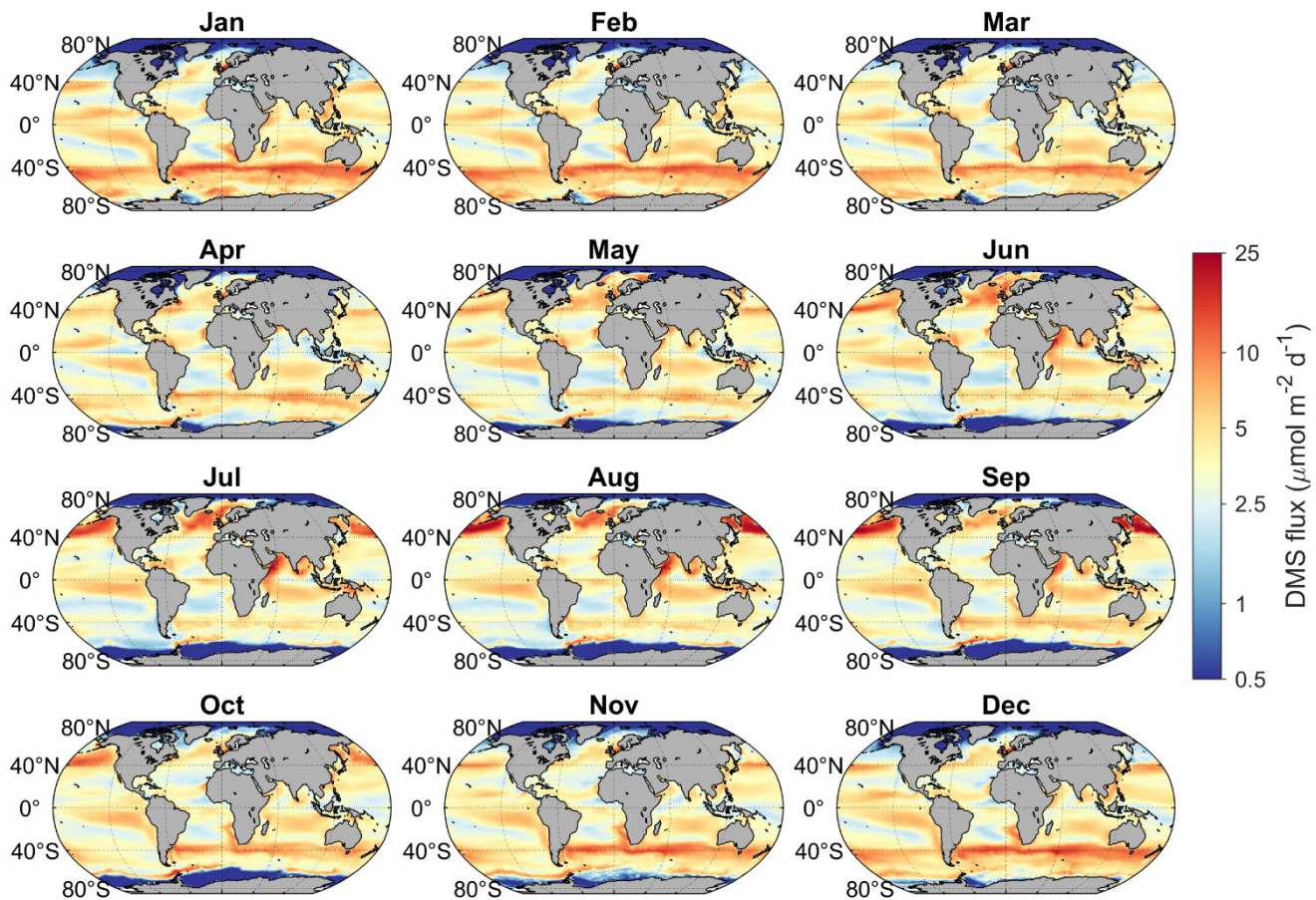
411 As shown in Fig. 409, the higher wind speeds in autumn and winter at mid- and high-latitudes result in higher total transfer  
 412 velocities, leading to smaller summer-to-winter ratios of DMS emission flux compared to that of DMS concentration. In low

413 latitudes, the existence of the trade wind zones in both hemispheres further leads to two high-flux bands ~~between 5° to 20°~~.  
414 The emission fluxes in the equatorial region between these two trade zones are significantly lower. Although the latitudinal  
415 distributions of mean DMS emission fluxes in the southern and northern hemispheres are almost symmetrical, the huge  
416 difference in ocean area between the two hemispheres results in a significantly higher total emission from the southern  
417 hemisphere. Since anthropogenic SO<sub>2</sub> emissions are mainly concentrated in the northern hemisphere, oceanic DMS plays a  
418 much more important role in the southern hemisphere, especially over the regions south of 40° S where the DMS emission is  
419 high and the perturbation of anthropogenic pollution is low.

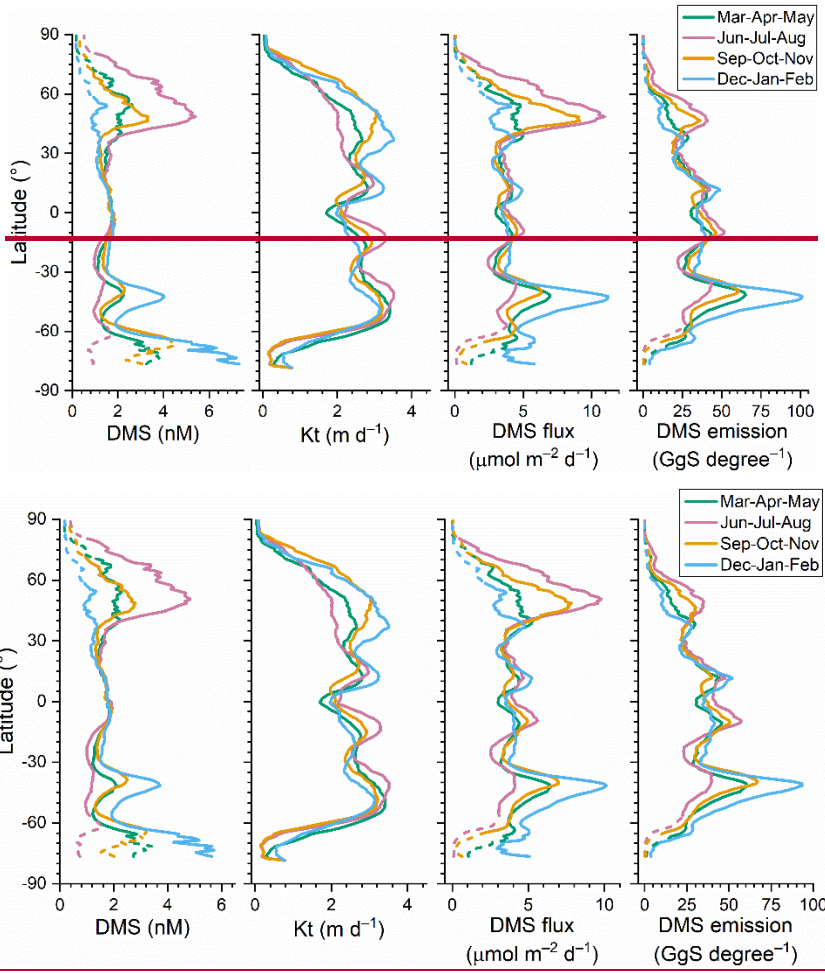
420 According to our newly built DMS gridded dataset, the global area-weighted annual mean concentration of DMS at the sea  
421 surface from 1998 to 2017 was  $\sim 1.72\text{--}71$  nM (1.67–1.76–75 nM), which is within the range among the values (1.6 to 2.4 nM)  
422 obtained by various methods in previous studies (Tesdal et al., 2016). The global annual mean DMS emission to the atmosphere  
423 was  $17.0\text{--}2$  TgS yr<sup>-1</sup> (16.69–17.45 TgS yr<sup>-1</sup>), with 10.3 TgS yr<sup>-1</sup> (60.659.9%) from the southern hemisphere and 6.79 TgS yr<sup>-1</sup>  
424 <sup>1</sup> (39.440.1%) from the northern hemisphere.

425





428  
429 **Figure 98.** Monthly climatology of global DMS sea-to-air flux from 1998 to 2017.  
430  
431



432 **Figure 409.** Latitudinal distributions of sea surface DMS concentration, total transfer velocity (Kt), sea-to-air flux, and total  
 433 emission in different seasons during 1998–2017. The dashed parts of the lines represent the missing ratio of satellite Chl *a* data  
 434 for DMS simulation is higher than 0.5, thus most Chl *a* data is from CMEMS global biogeochemical multi-year hindcast.  
 435  
 436  
 437

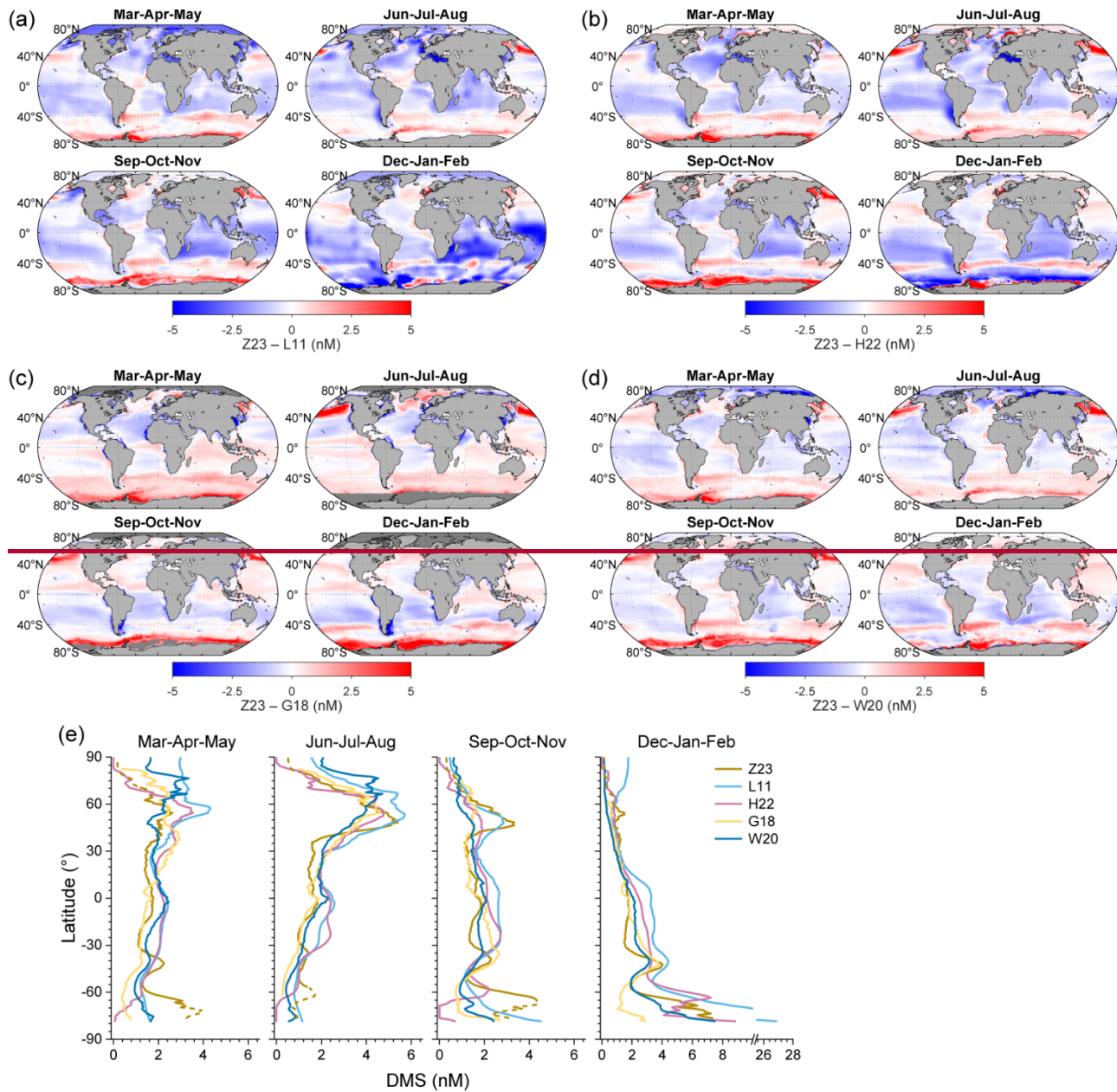
### 438 3.2.2 Comparisons with other global DMS climatologies

439 Here we compare the distributions of DMS concentration derived from our ANN simulation (referred to as Z23) with four  
 440 previously constructed climatologies (Fig. 440), including (1) L11: the widely used second version of  
 441 interpolation/extrapolation-based climatology established by Lana et al. (2011), (2) H22: an updated version of L11  
 442 incorporating much more DMS measurements and using dynamic biogeochemical provinces (Hulswar et al., 2022), (3) G18:  
 443 the DMS concentration field estimated by a two-step remote sensing algorithm (Galí et al., 2018), and (4) W20: the previous  
 444 DMS climatology simulated by ANN (Wang et al., 2020).

445 Overall, all datasets exhibit the general pattern of high DMS concentration during summer and low concentration during winter,  
446 but notable distinctions emerge in their specific distributions. Due to the limitation of the method used,  $DMS_{L11}$  exhibits  
447 relatively lower spatial heterogeneity (i.e., higher patchiness), which may not well capture the detailed spatial variability on a  
448 regional scale. Compared with  $DMS_{L11}$ ,  $DMS_{Z23}$  is significantly lower at high latitudes during summer and in the South Indian  
449 Ocean and Southwest Pacific Ocean from December to February (Fig. 44a10a). Particularly in the southern polar region  
450 (Polar\_S), latitudinal averages of  $DMS_{L11}$  surpass 10 nM during summer, which are 1–3 times higher than  $DMS_{Z23}$  (Fig.  
451 44e10e). However,  $DMS_{Z23}$  maintains a similar level around the Antarctic in March compared to summer, and it is significantly  
452 higher than  $DMS_{L11}$  as well as other three climatologies.  $DMS_{H22}$  shows lower disparities with  $DMS_{Z23}$  in the Arctic, the South  
453 Indian Ocean, and the Southwest Pacific Ocean, but the summertime concentrations in most of Polar\_S region are also  $> 2$  nM  
454 higher than  $DMS_{Z23}$  (Fig. 44b10b). In contrast,  $DMS_{H22}$  in Polar\_S from September to November is  $\sim 2$  nM lower than  
455  $DMS_{Z23}$ . The global area-weighted annual mean DMS concentrations in L11 and H22 are 2.43 nM and 2.26 nM, respectively,  
456 which are approximately 41.342.1% and 31.432.2% higher than Z23.

457 G18 exhibits the lowest global annual mean concentration (1.63 nM) among these climatologies, approximately 5.24.7% lower  
458 than Z23. The most notable deviation occurs in the North Pacific during boreal summer and near the Antarctic during austral  
459 summer and autumn, where  $DMS_{Z23}$  is  $> 3.5$  nM ( $> 100\%$ ) higher than  $DMS_{G18}$  (Fig. 44e10c). Conversely, there are high DMS  
460 concentrations ( $> 5$  nM) in certain coastal seas (such as the coasts of East and Northeast Asia, the coasts of Patagonia and  
461 Peru, the southwestern coast of Africa, and the western coasts of the Sahara Desert and North America and the Sahara Desert)  
462 based on the G18 estimate. This characteristic is not fully replicated by other DMS fields, possibly due to the underestimation  
463 of DMS by our model and other methods in coastal regions as well as the overestimation of Chl *a* by satellites in coastal  
464 regions caused by the interference of colored dissolved organic matters and non-algal detrital particles (Aurin and Dierssen,  
465 2012). W20 exhibits the highest consistency with Z23 in spatiotemporal distribution patterns as well as the lowest difference  
466 in global annual mean concentration (1.74 nM, only 1.28% higher than Z23). However, notable discrepancies exist in specific  
467 regions. For instance, during summertime,  $DMS_{Z23}$  is  $> 1$  nM ( $> 40\%$ ) lower than  $DMS_{W20}$  in more than half of the Arctic area,  
468 while in North Pacific and Southern Ocean  $DMS_{Z23}$  is significantly higher than  $DMS_{W20}$  (Fig. 44d10d). Furthermore, only  
469  $DMS_{Z23}$  forms a nearly complete high-concentration annular band at  $\sim 40^\circ$  S during austral summer.

470



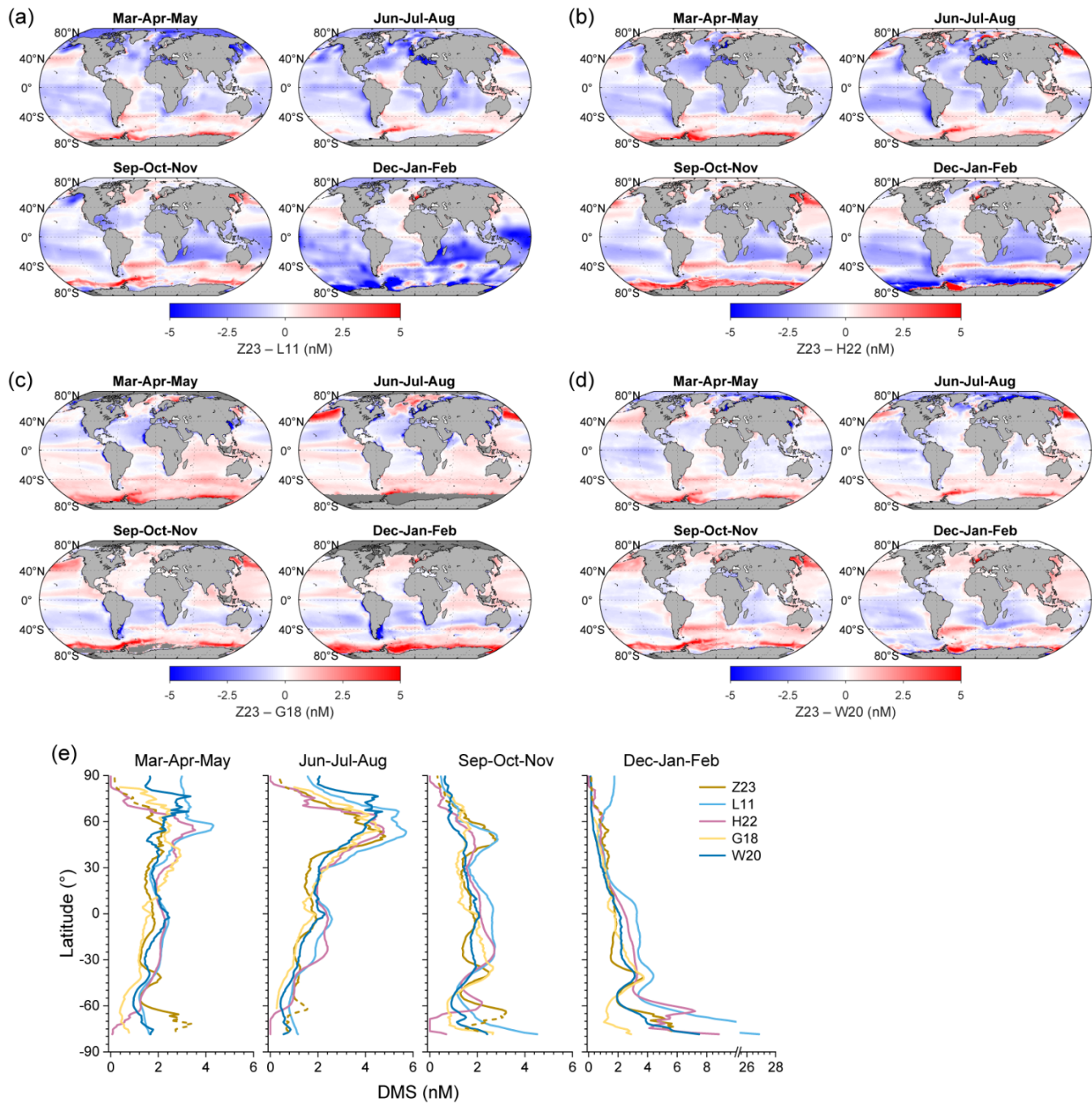


**Figure 110.** (a–d) The spatial distributions of DMS concentration differences between Z23 and four previously estimated fields across different seasons: (a) L11, (b) H22, (c) G18, and (d) W20. Dark gray regions in the ocean represent data missing in at least one field. (e) Comparisons between the latitudinal distributions of Z23 and four previous DMS fields across different

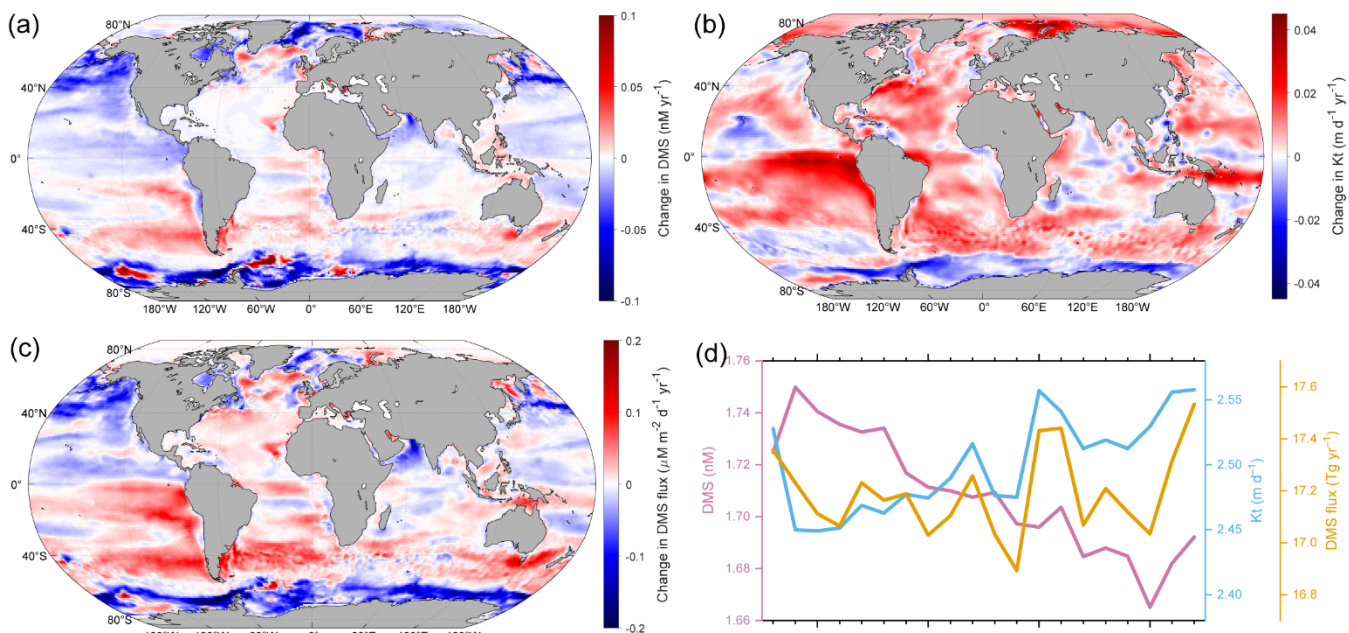
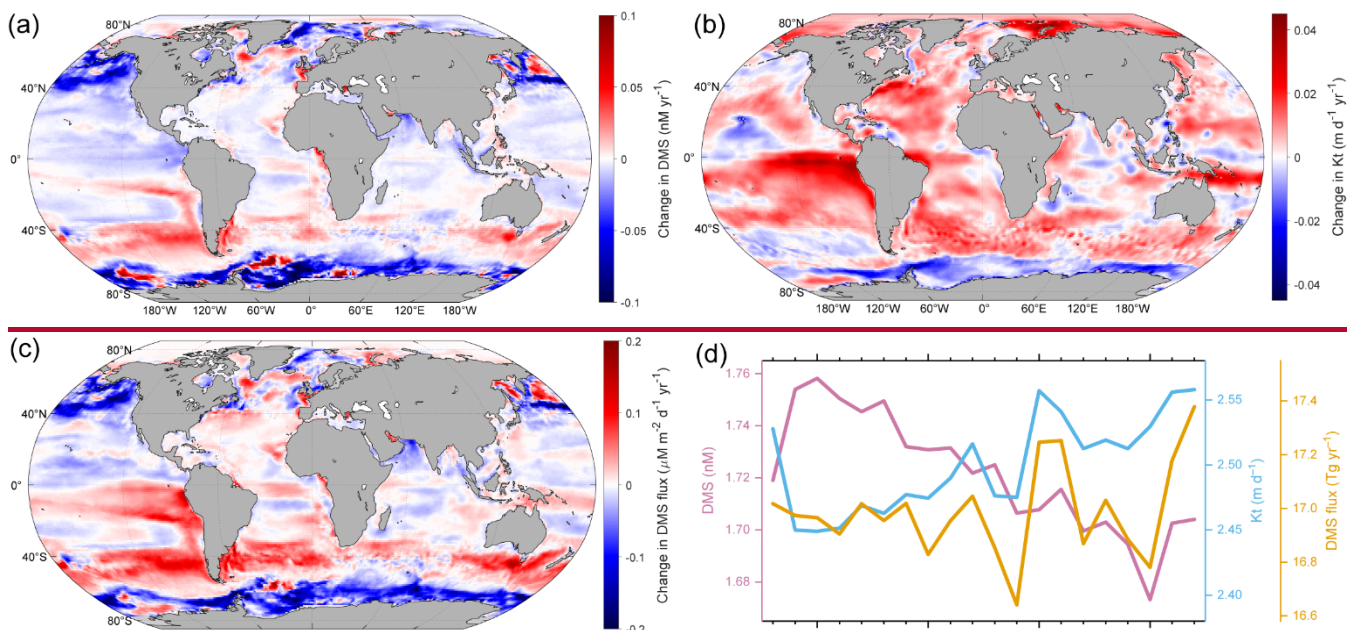
476 seasons. The dashed parts of the Z23 lines represent the missing ratio of satellite Chl  $\alpha$  data for DMS simulation is higher than  
477 0.5, thus most Chl  $\alpha$  data is from CMEMS global biogeochemical multi-year hindcast.  
478

### 479 3.2.3 Decadal changes

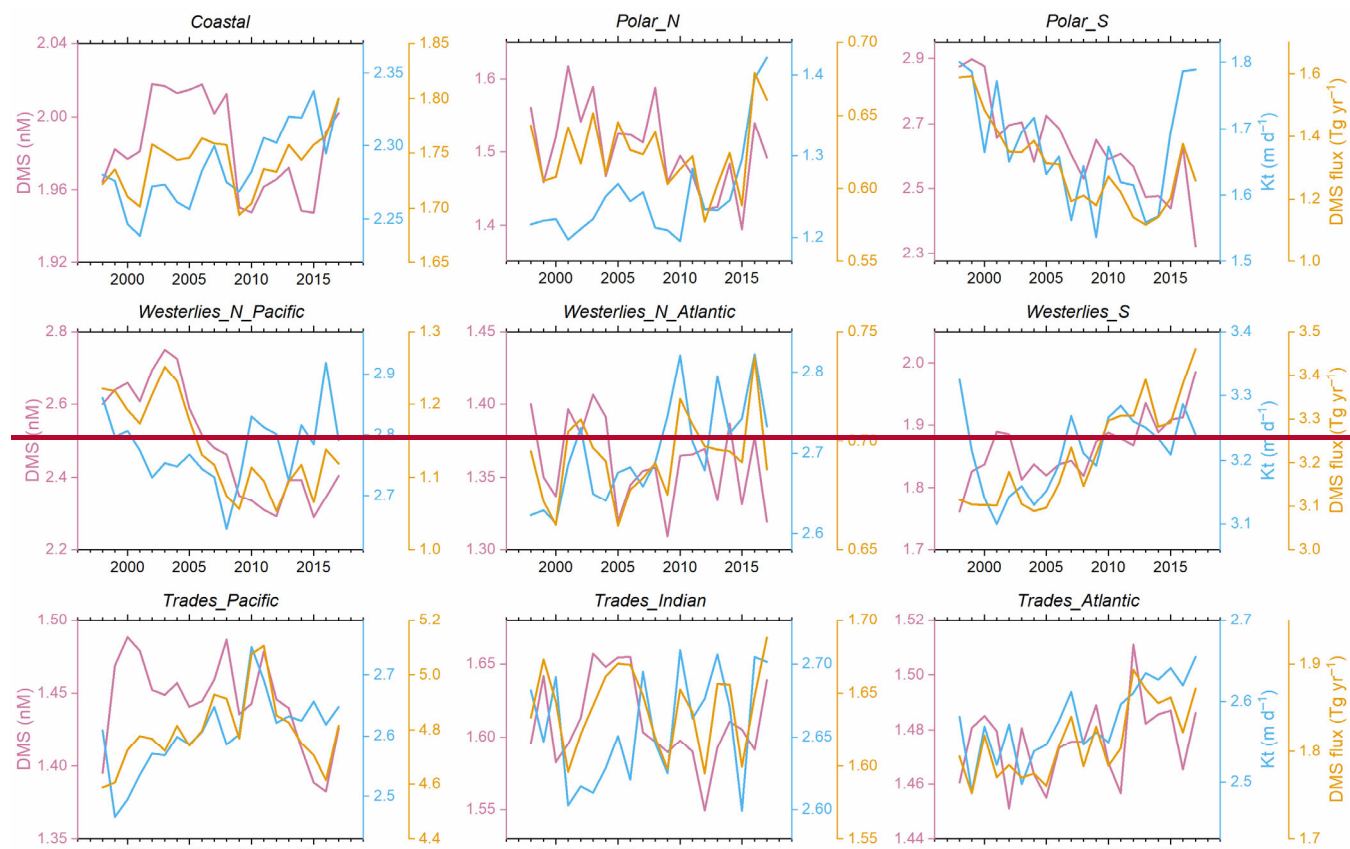
480 One of the advantages of our ANN-derived DMS dataset is its time-resolved nature, which enables us to investigate the  
481 interannual variations in sea surface DMS concentration and flux. Here we present the decadal trends of DMS concentration,  
482 Kt, and emission flux spanning from 1998 to 2017 at both global and regional scales. Overall, the absolute interannual  
483 variability of DMS concentration across most global oceanic regions appears relatively small. ~~85.3~~<sup>88.4</sup>% of the global oceanic  
484 area exhibited a difference range of less than 1 nM between the maximum and minimum annual average concentrations during  
485 this 20-year period, particularly evident in tropical and subtropical regions with latitudes between 40° S and 40° N. At latitudes  
486 higher than 40° in both hemispheres, notable decadal changes occurred (Fig. [12a](#)[11a](#)). Annual mean DMS concentrations in  
487 the Greenland Sea, the North Pacific, and the Southern Ocean exhibited significant decreasing trends with rates exceeding  
488 0.03 nM yr<sup>-1</sup> ( $P < 0.05$ ). A significant decreasing trend was also noted in the eastern tropical Pacific Ocean, albeit at a much  
489 lower absolute rate, primarily below 0.015 nM yr<sup>-1</sup>. Conversely, there were significant increasing trends in the Labrador Sea,  
490 the South Pacific (35° S – 60° S, 150° E – 75° W), and the southeastern Pacific, with the highest rate exceeding 0.02 nM yr<sup>-1</sup>.  
491 The global annual mean concentration exhibited a decreasing trend with a rate of ~~0.0033~~<sup>0.0035</sup> nM yr<sup>-1</sup> ( $P < 0.05$ , Fig. 11d).  
492 The highest value (1.~~76~~<sup>75</sup> nM) occurred in [2000](#)[1999](#), and the lowest concentration (1.67 nM) occurred in 2015. Due to the  
493 primary influences of increasing WS and secondary impact of rising SST in most mid- and low-latitude regions (Fig. [S8](#)[S11](#)),  
494 the Kt of DMS also showed an overall increasing trend, especially in the eastern Pacific and Atlantic Ocean (Fig. [12b](#)[11b](#)).  
495 The increase in Kt can offset the decrease in DMS concentration to some extent, resulting in no significant trend in global  
496 DMS emissions during this 20-year period (Fig. [12d](#)[11d](#)).

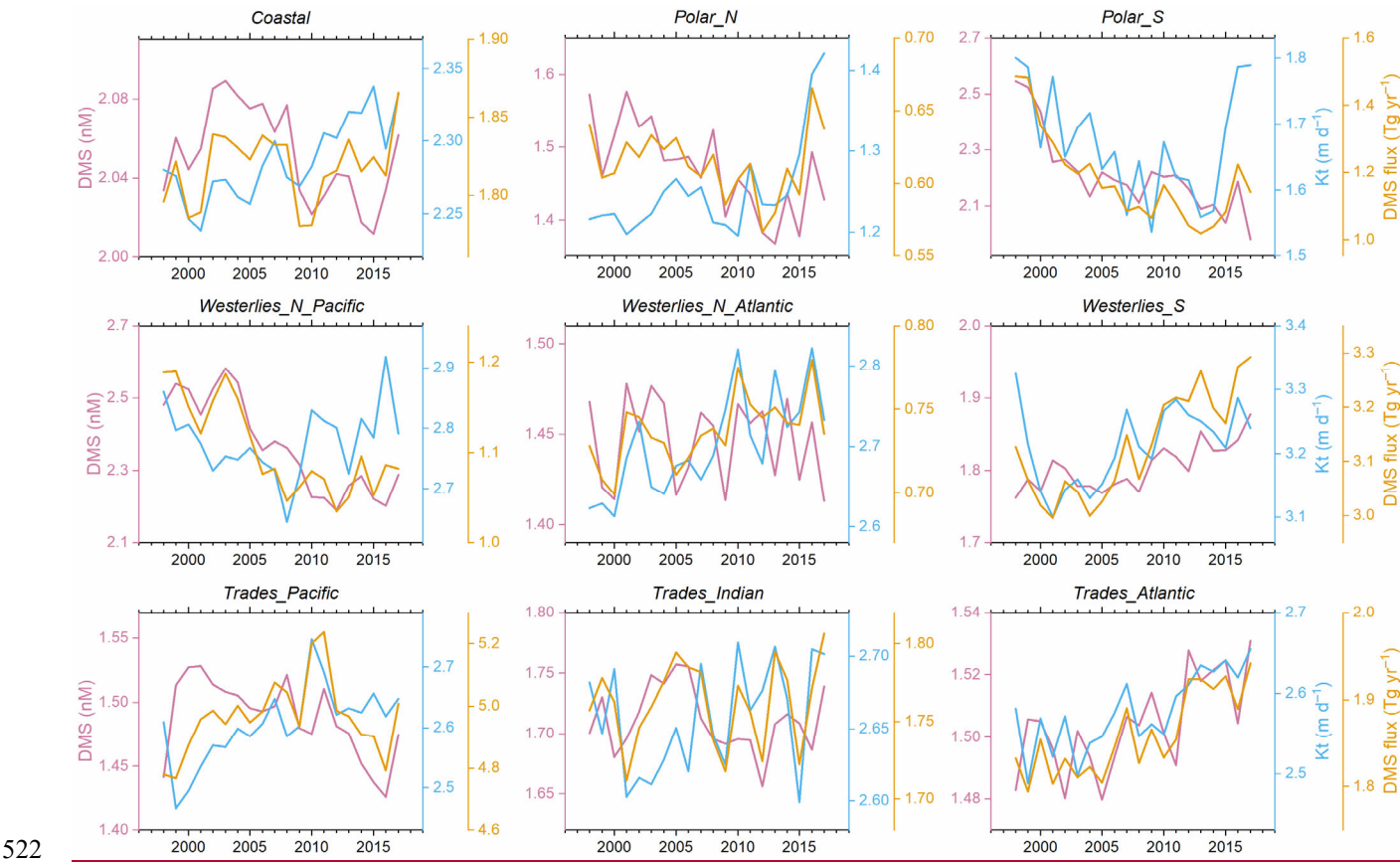
497 In the Arctic region, which stands as one of the most sensitive areas to climate warming (Screen et al., 2012; Serreze and  
498 Barry, 2011), the sea ice coverage has undergone significant reduction over the past ~~2~~two decades, particularly noticeable in  
499 the Barents Sea and Kara Sea, and further north ( $> 1\% \text{ yr}^{-1}$  for annual mean SI, Fig. [S8](#)[S11](#)). The retreat of summertime sea  
500 ice leads to an expansion of open-sea surface, potentially amplifying DMS emission (Galí et al., 2019). However, despite this  
501 trend, there was no significant increase in the annual total emission from the Polar\_N region over the same period, primarily  
502 due to a decreasing trend in DMS concentration (Fig. [13](#)[12](#)). On the other hand, the highest emission took place in the last two  
503 years ( $> 0.65$ ~~64~~ Tg yr<sup>-1</sup>), attributed to the highest Kt. Thus, it is likely that a rise in DMS emission will appear in future Arctic  
504 region with further loss of sea ice coverage (Galí et al., 2019). In contrast to the Arctic, the Southern Ocean has experienced a  
505 significant increase in sea ice fraction (Fig. [S8](#)[S11](#)), leading to a significant decrease in Kt (Fig. [12b](#)[11b](#)). Coupled with the  
506 decreased DMS concentration, it resulted in a substantial decline in the DMS emission flux (Fig. [12e](#)[-11c](#) and [13](#)[12](#)). The  
507 highest annual total emission flux in the Polar\_S region occurred in 1998 (1.~~42~~<sup>49</sup> TgS), while the lowest occurred in 2013

508 (1.~~42~~02 TgS), representing a decrease of  $\sim$ ~~24~~32%. Across other oceanic regions, the annual average DMS concentrations in  
509 the Westerlies\_N\_Pacific and Trades\_Pacific regions exhibit decreasing trends over the past 20 years, while the concentration  
510 in Westerlies\_S and Trades\_Atlantic has increased ( $P < 0.05$ , Fig. ~~13~~12). Regarding DMS flux, the Westerlies\_N\_Pacific  
511 showed a decrease, while the Westerlies\_N\_Atlantic, Westerlies\_S, and Trades\_Atlantic showed an increase. There was no  
512 significant trend in other low-and mid latitude regions.



516 **Figure 1211.** (a–c) The spatial distributions of changes in (a) DMS concentration, (b) Kt, and (c) DMS emission flux from  
 517 1998 to 2017. The linear regression slopes for the annual means are taken as the changing rates here. (d) The temporal changes  
 518 of global annual mean DMS concentration, Kt, and total emission flux from 1998 to 2017.





522 **Figure 1312.** The temporal changes of annual mean DMS concentration,  $K_t$ , and total emission flux in different regions from  
 523 1998 to 2017.

524 **3.3 Connection with atmospheric biogenic sulfur**

525 One of the primary objectives of developing this daily gridded DMS dataset (Z23) spanning multiple years is to improve the  
 526 emission inventory of marine biogenic DMS, thereby enhancing the modelling performance for atmospheric sulfur chemistry,  
 527 especially for simulating sulfur-containing aerosols. To assess whether our newly constructed DMS dataset can reach this  
 528 objective, we employed a backward trajectory-based method to examine the correlation between sea surface DMS emissions  
 529 and resulting DMS oxidation products in the atmosphere. The correlation was then compared against those derived from  
 530 previously reported DMS climatologies (i.e., L11, H22, G18, and W20).

531  
 532 Here we use the observed concentrations of particulate methanesulfonic acid (MSA) over the Atlantic Ocean as a reference.  
 533 MSA is one of the major end-products of DMS in the atmosphere and is solely from the oxidation of marine biogenic DMS  
 534 over remote oceans (Saltzman et al., 1983; Savoie et al., 2002; Osman et al., 2019). Therefore, there is likely to be a dependence

535 of the variation of MSA concentration on the DMS emission fluxes. During four transection cruises in the Atlantic conducted  
536 by *R/V Polarstern* (20 April – 20 May 2011, 28 October – 1 December 2011, 10 April – 15 May 2012, and 27 October – 27  
537 November 2012), the MSA concentrations in submicron aerosols were measured online using a High-Resolution Time-of-  
538 Flight Aerosol Mass Spectrometer. The ship tracks are shown in Fig. [S9S12](#), and detailed information about the cruises and  
539 measurement methodology was provided by Huang et al. (2016). The 72-hour air mass backward trajectories reaching the ship  
540 position were calculated every hour by the HYSPLIT model, starting from a height of 100 m (Stein et al., 2015). Subsequently,  
541 the air mass exposure to DMS emission (AEDMS), denoting the weighted average of DMS emission flux along the trajectory  
542 path, was calculated following the approach of Zhou et al. (2021). We used 5 different DMS gridded datasets, including Z23,  
543 L11, H22, G18, and W20. For Z23, the calculated daily DMS fluxes were utilized. For the remaining 4 monthly climatologies,  
544 we applied the daily Kt data from Z23 to calculate the DMS fluxes, thus eliminating the potential confounding influences  
545 stemming from different Kt parameterizations. In this calculation, the same concentration was assigned to all days within a  
546 month without interpolation. Detailed procedures for the calculation of AEDMS are elucidated in Appendix C.

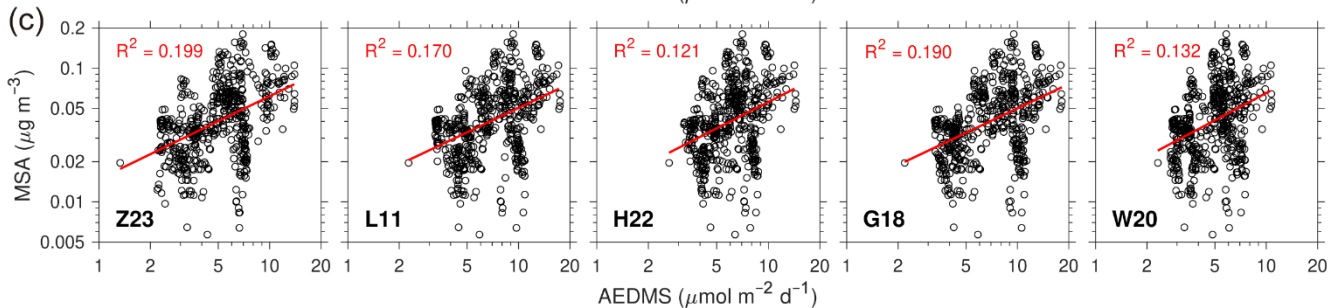
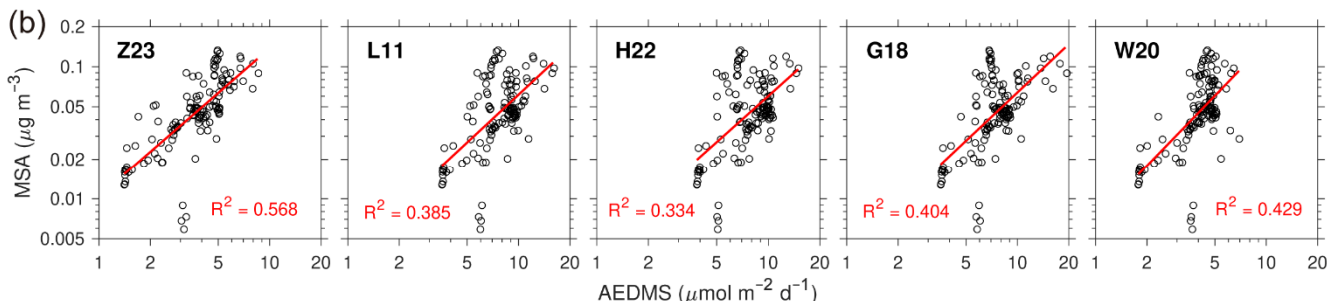
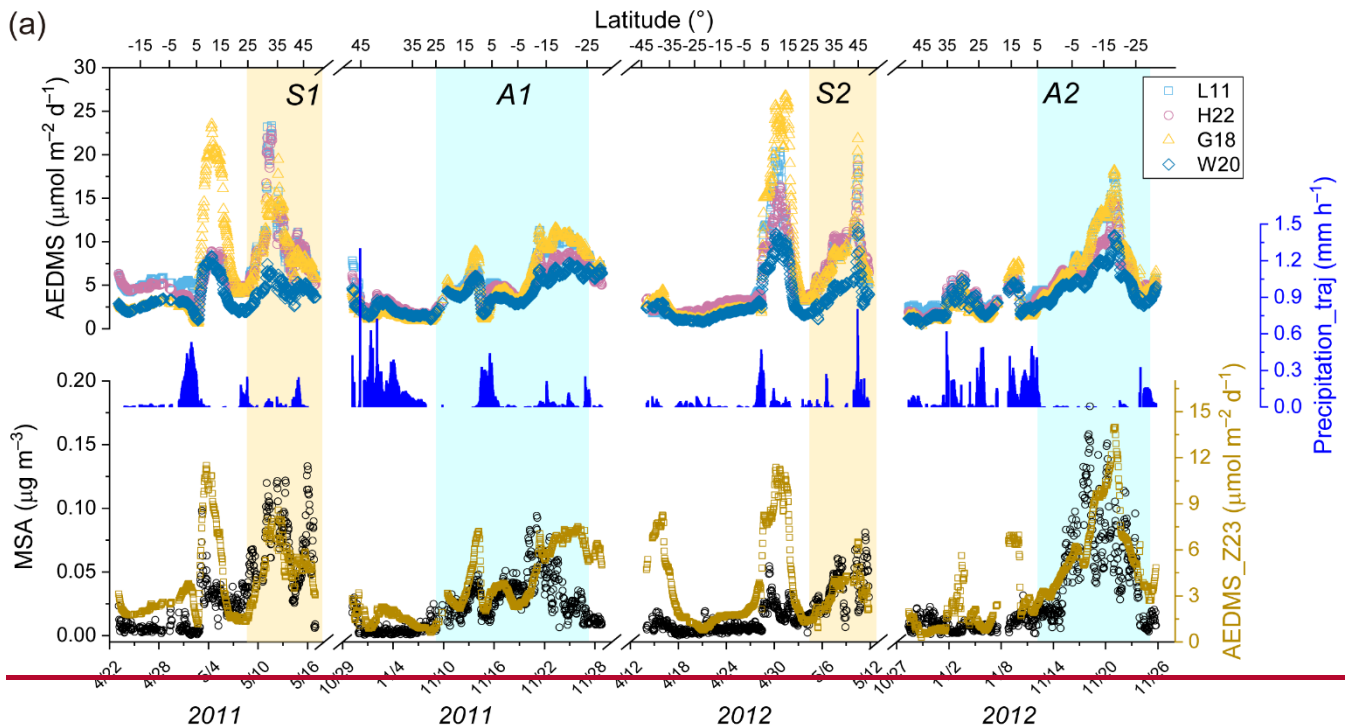
547 MSA concentrations were significantly higher in late spring than those in autumn for both North and South Atlantic Oceans  
548 (Fig. [14a13a](#)). For example, during the boreal spring cruise in 2011, the average MSA concentration over the North Atlantic  
549 ( $0.068 \mu\text{g m}^{-3}$ , north of  $25^\circ \text{N}$ ) was about an order of magnitude higher than the average concentration over the South Atlantic  
550 ( $0.006 \mu\text{g m}^{-3}$ , south of  $5^\circ \text{S}$ ). During the boreal autumn cruise in 2011, the average concentration over the South Atlantic  
551 ( $0.034 \mu\text{g m}^{-3}$ , south of  $5^\circ \text{S}$ ) was  $\sim 5$  times higher than that over the North Atlantic ( $0.006 \mu\text{g m}^{-3}$ , north of  $25^\circ \text{N}$ ). In addition  
552 to this major seasonal pattern, there was also a minor MSA concentration peak between  $5^\circ$ – $15^\circ \text{N}$  in both seasons. The spatial  
553 and seasonal variations of AEDMS based on the Z23 dataset (referred to as AEDMS\_Z23) largely coincided with these MSA  
554 concentration patterns (Fig. [14a13a](#)). It should be noted that the MSA/AEDMS ratio between  $5^\circ$ – $15^\circ \text{N}$  was significantly lower  
555 than those in other high-MSA regions, which may result from the DMS simulation biases near the coast of West Africa or the  
556 lower DMS-to-MSA conversion yields related with air temperature and oxidant species (Barnes et al., 2006; Bates et al., 1992).  
557 There were also several AEDMS peaks in North Atlantic during November 2012, inconsistent with the continuously low MSA  
558 concentrations. Given the high precipitation rates along the trajectory (Fig. [14a13a](#)), a strong wet scavenging process might  
559 significantly reduce aerosol concentrations (Wood et al., 2017).

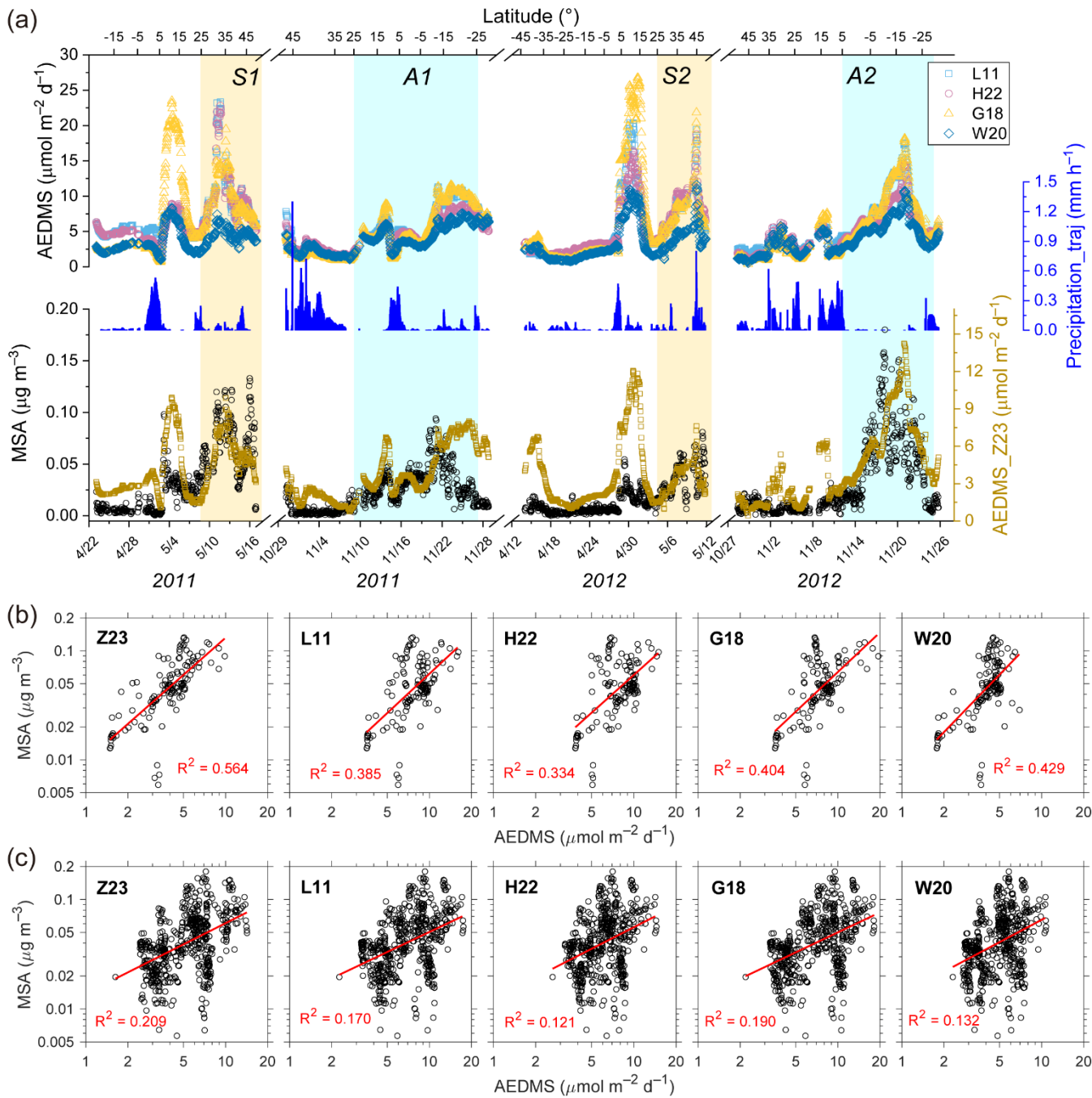
560 The AEDMS derived from other DMS concentration fields showed similar variations to AEDMS\_Z23 (Fig. [14a13a](#)). It is not  
561 surprising since all DMS concentration fields exhibit similar large-scale spatiotemporal patterns, and identical air mass  
562 transport path and Kt were applied in different AEDMS calculations. However, due to the lower temporal resolutions and  
563 absence of interannual changes in those DMS monthly climatologies, the resulting AEDMS may be less effective in capturing  
564 variability at finer scales or across different years. Here we focus on the high-MSA periods to elaborate on this issue, which  
565 corresponds to latitudes north of  $25^\circ \text{N}$  in boreal spring (S1 and S2 in Fig. [14a13a](#)),  $25^\circ \text{N}$  –  $25^\circ \text{S}$  in boreal autumn of 2011  
566 (A1 in Fig. [14a13a](#)), and south of  $5^\circ \text{N}$  in boreal autumn of 2012 (A2 in Fig. [14a13a](#)). As shown in Fig. [14b13b](#), hourly MSA

567 concentrations exhibited significantly stronger correlations with AEDMS\_Z23 than with other AEDMS time series in S1 and  
568 S2, indicating AEDMS\_Z23 can explain more (1.~~32~~<sub>31</sub>–1.~~70~~<sub>69</sub> times) variance of MSA concentration. During A1 and A2,  
569 the correlations between AEDMS and MSA concentration were weaker than those during S1 and S2, possibly due to higher  
570 DMS prediction biases in South Atlantic or different influencing factors on atmospheric DMS chemistry across wide spatial  
571 ranges. Nonetheless, AEDMS\_Z23 still exhibited the highest correlation with MSA (Fig. [14e](#)[13c](#)). This overall stronger  
572 connection between Z23 and atmospheric DMS-derived aerosols mainly benefited from the combined effects of higher time  
573 resolution and inherent interannual variations. For example, the ratio of average MSA concentration during S1 to that during  
574 S2 (S1-to-S2 ratio) was 1.89, and the A2-to-A1 ratio was 1.75. AEDMS\_Z23 exhibited a slightly lower but still significant  
575 interannual variation degree, where the S1-to-S2 ratio and A2-to-A1 ratio were 1.~~60~~<sub>58</sub> and 1.~~45~~<sub>46</sub>, respectively. However,  
576 this interannual variation cannot be reproduced by other datasets, where the S1-to-S2 ratio and A2-to-A1 ratio were in the  
577 range of 1.08–1.30 and 1.19–1.29, respectively. These results manifest the potential of our newly developed DMS gridded  
578 data product to enhance the modeling performance for atmospheric DMS processes compared with previously reported  
579 climatologies.

580 It is worth noting that the satellite-based algorithms of G18 and ANN model of W20 can also be utilized to produce daily  
581 multiyear DMS fields as Z23. Future investigations could include comparisons with these fields, facilitating a more  
582 comprehensive assessment of the performance of each algorithm/model. Furthermore, the AEDMS method used here is a  
583 highly simplified approach without considering the complex DMS chemistry in the atmosphere, and the intercomparisons  
584 based on chemical transport models can be used in the future to obtain a more straightforward conclusion.

585





587

588 **Figure 4413.** (a) Time series of observed MSA concentration, AEDMS calculated based on different DMS concentration  
 589 datasets, and average precipitation along the backward trajectory (Precipitation\_traj) during four Atlantic cruises in 2011–  
 590 2012. (b–c) Correlations between hourly MSA concentration and AEDMS based on different DMS concentration datasets (b)

591 during periods S1 + S2 and (c) during periods A1 + A2. Data points during the periods with air mass time fraction within the  
592 boundary layer less than 90% or Precipitation\_traj larger than 0.05 mm h<sup>-1</sup> were removed.

593 **4 Uncertainties and limitations**

594 Although our ANN ensemble model and derived DMS dataset demonstrate certain advantages compared to previous studies,  
595 as discussed in Section 3.3, there persist notable uncertainties and limitations, which result in the ~3935% uncaptured variance  
596 (Fig. 4a3a) and non-negligible simulation biases, e.g., underestimation of extremely high DMS concentrations and  
597 overestimation of low DMS concentrations. Firstly, there is a mismatch in the spatial and temporal scales between the input  
598 and target. The target, sea surface DMS concentrations, are obtained from in-situ measurements taken at specific locations and  
599 time points. In contrast, the input data are primarily from gridded datasets where each pixel represents an average over a  
600 defined spatial and temporal range. This is particularly significant for the ECCO variables, which have the largest spatial grid  
601 size of 110 km. Consequently, extreme values at specific locations cannot be accurately captured by the regional averages,  
602 resulting in damped variations among the samples. FirstlySecondly, the data of input featuresinput data from different  
603 sources and the observed sea surface DMS concentrations inherently possess certain uncertainties, which can introduce biases  
604 noises into the ANN learning process. Thirdly, the ANN itself may not be powerful enough to fully capture the complex input-  
605 output relationships across different oceanic regions, especially when the samples are scarce under specific environmental  
606 conditions. Finally, beyond the 9 variables incorporated in this study, other environmental parameters such as pH (Six et al.,  
607 2013; Hopkins et al., 2010) and trace metal elements (Li et al., 2021) can also influence DMS concentration. Not incorporating  
608 these factors may introduce additional biases.

609 The overall bias for  $\log_{10}$ DMS is at a similar level between high- and low-concentration ends, but the DMS concentration on  
610 a linear scale is more underestimated in the high-concentration regime than it is overestimated in the low-concentration regime.  
611 As a result, our simulation results may tend to underestimate the annual average DMS concentration and flux. To mitigate this  
612 critical bias and reduce model uncertainty, high-quality input datasets with finer spatial resolution are needed in the future.  
613 The high-time resolution nature of the resulted daily DMS data product would be more valuable if accompanied by higher  
614 spatial resolution. Expanding the data volume is also crucial for improving model performance. Although the current DMS  
615 observational data covers all major oceanic basins, certain regions such as the Trades Pacific remain underrepresented.  
616 Advances in online measurement technologies offer promising avenues for acquiring more extensive and convenient  
617 observational data (Hulswar et al., 2022). In the future, more observations are imperative for these underrepresented regions,  
618 facilitating model refinement and updates. Additionally, incorporating more input features to the model would be beneficial.  
619 This necessitates a comprehensive understanding of the spatiotemporal distributions of those input features, and further field  
620 measurements are important to this end. Moreover, integrating DMS biogeochemical mechanisms with machine learning  
621 technique, i.e., a hybrid model coupling physical processes with data-driven approach, may further improve prediction

622 accuracy, generalization, and interpretability (Reichstein et al., 2019). Secondly, ANN models may not fully capture all intricate  
623 data patterns, and the outcomes from each training may exhibit certain randomness. In this study, the average standard  
624 deviation of simulated  $\log_{10}$ DMS values from 100 neural networks is 0.244, and the 5%–95% range of the coefficient of  
625 variation for DMS concentration is 0.18–2.54, with an average of 0.72. If the detailed uncertainties associated with each data  
626 source are known, future investigations could employ Monte Carlo methods to estimate the uncertainties of final results arising  
627 from the aforementioned two factors (Abdar et al., 2021; Moradkhani et al., 2012). Thirdly, although the DMS observational  
628 data covers all major oceanic basins, certain regions such as the Trades Pacific remain underrepresented. Advances in online  
629 measurement technologies offer promising avenues for acquiring more extensive and convenient observational data (Hulswart  
630 et al., 2022). In the future, more observations are imperative for these underrepresented regions, facilitating model refinement  
631 and updates. Fourthly, as discussed in Section 3.1, the model cannot well reproduce the extremely high and extremely low  
632 DMS concentrations, which potentially introduces notable biases, particularly in flux calculations. We also need more  
633 observational data to help mitigate this issue.

634 Beyond the 9 variables incorporated in this study, other environmental parameters, such as pH (Six et al., 2013; Hopkins et  
635 al., 2010) and trace metal elements (Li et al., 2021), can also influence DMS concentration. Not incorporating these factors  
636 may introduce potential biases. Thus, further field measurements of trace metals are necessary to comprehend their  
637 spatiotemporal distributions, which are likely to enhance the model's ability to simulate sea surface DMS concentrations. In  
638 terms of the temporal resolution, our product significantly surpasses previous monthly climatologies. However, the higher  
639 temporal resolution would be even more valuable if accompanied by higher spatial resolution. In this work, the spatial  
640 resolution is limited by the ECCO dataset, where the largest spatial grid size is 110 km. Therefore, we are not able to achieve  
641 higher spatial resolution without interpolation. Enhancing the spatial resolution of DMS fields using high-quality input datasets  
642 with finer spatial resolution represents a prospective direction for future research.

643 When using our newly developed DMS dataset, there are two issues that need to be noted. Firstly, there is a significant portion  
644 of missing satellite Chl *a* data during winter in polar regions. In such instances, the modeling data from CMEMS global  
645 biogeochemical multi-year hindcast was used, which may introduce higher uncertainty. We have provided the flags indicating  
646 the source of Chl *a* data for each grid in the dataset. Nevertheless, given the low phytoplankton biomass and extensive sea ice  
647 coverage during winter, DMS emissions are typically at the lowest level of the year, thus the satellite data missing has a  
648 relatively small impact on investigating the subsequent effects of DMS emission on atmospheric environment. Secondly, since  
649 the ANN ensemble model exhibits limited capacity in accurately reproducing extremely high concentrations of DMS, the DMS  
650 concentrations in certain nearshore areas with intensive biological activity may be greatly underestimated.

651

652 **5 Code and data availability**

653 The generated gridded datasets of DMS concentration, total transfer velocity, and flux have been deposited at  
654 <https://doi.org/10.5281/zenodo.11879900> <https://zenodo.org/records/10906101> (Zhou et al., 2024) and can be downloaded  
655 publicly. The ANN model code and the Matlab scripts for data analysis are available from  
656 <https://doi.org/10.5281/zenodo.12398985> <https://zenodo.org/record/10937598> (Zhou, 2024).

657 **6 Conclusion**

658 Based on the global sea surface DMS observations and associated data of 9 relevant environmental variables, an ANN  
659 ensemble model was trained. The ANN model effectively captures the variability of DMS concentrations and demonstrates  
660 good simulation accuracy. Leveraging this ANN model, a global sea surface DMS gridded dataset with a daily resolution  
661 spanning 20 years (1998–2017) was constructed. The global annual average concentration was  $\sim 1.72-71$  nM, falling within  
662 the range of previous estimates, and the annual total emission was  $\sim 17.0-2$  TgS yr $^{-1}$ . High DMS concentrations and fluxes took  
663 place during summer in North Pacific (40°–60° N), North Atlantic (50°–80° N), the annular band around 40° S, and the  
664 Southern Ocean. With this newly developed dataset, the day-to-day changes and interannual variations can be investigated.  
665 The global annual average concentration shows a mild decreasing trend ( $\sim 0.0033-0.0035$  nM yr $^{-1}$ ), while the total emission  
666 remains stable. There were more significant decadal changes in certain regions. Specifically, the annual DMS emission in the  
667 South Pacific and North Pacific showed opposite trends.

668 To further validate the robustness and advantages of our new dataset, an airmass trajectory-based approach was applied to link  
669 the DMS flux and atmospheric MSA concentration. Compared to previous monthly climatologies, the airmass exposure to  
670 DMS calculated using our new dataset explains a greater amount of variance in atmospheric MSA concentration over the  
671 Atlantic Ocean. Therefore, despite the presence of uncertainties and limitations, the new dataset holds the potential to serve as  
672 an improved DMS emission inventory for atmospheric models and enhance the simulation of DMS-induced aerosols and their  
673 associated climatic effects.

674

675 **Appendix A: Acronyms**

676 AEDMS Air mass exposure to DMS emission

677 ANN Artificial neural network

678 BLH Boundary layer height

679 CCN Cloud condensation nuclei

680 Chl  $\alpha$  Chlorophyll  $\alpha$

681 DMS Dimethyl sulfide

682 DMSP Dimethylsulfoniopropionate

683 DO Dissolved oxygen

684	DSWF	Downward short-wave radiation flux
685	ECCO	Estimating the Circulation and Climate of the Ocean
686	GSSD database	Global Surface Seawater DMS database
687	Kt	Total transfer velocity
688	MLD	Mixed layer depth
689	MB	Mean bias
690	MSA	Methanesulfonic acid
691	MSE	Mean square error
692	NAAMES	North Atlantic Aerosols and Marine Ecosystems Study
693	NMB	Normalized mean bias
694	RMSE	Rooted mean square error
695	PDF	Probability distribution function
696	SI	Sea ice fraction
697	SST	Sea surface temperature
698	SSS	Sea surface salinity
699	WS	Wind speed

700

701 **Appendix B: The weighted resampling strategy**

702 Apart from the data imbalance between coastal and non-coastal regions, there exists an imbalance across different DMS  
 703 concentration ranges. The majority of DMS concentrations (78.6%) fall within the range of 0.8 to 10 nM ( $\log_{10}(\text{DMS})$  between  
 704 -0.1 to 1). Samples with DMS concentrations exceeding 15 nM or falling below 0.3 nM only represent 6.9% of the entire  
 705 sample set. A weighted resampling strategy was applied to mitigate this imbalance (Fig. S7). We randomly sampled 50,000  
 706 samples with replacement from the original sample set. The probability of each sample being selected is proportional to the  
 707 weighting factor shown as the red dash line in Fig. S7b, which is dependent on its DMS concentration. Deriving the weighting  
 708 factors for weighted resampling

709 First, the probability distribution of initial  $\log_{10}(\text{DMS})$  values was fitted with a gamma distribution. The probability  
 710 density function, which is given below and displayed as the blue line in Fig. S7b.

$$711 f(x) = \frac{1}{\Gamma(k)\theta^k} (x + 4)^{k-1} e^{-(x+4)/\theta} \quad (\text{A1})$$

712 Here  $k$  and  $\theta$  represent the shape parameter and scale parameter, in this case, 100.7 and 0.044, respectively.  $x$  is the  $\log_{10}(\text{DMS})$   
 713 value. Since gamma distribution only takes positive values, we added 4 to the original  $x$  as the dependent variable for  
 714 distribution fitting. We then obtained a new gamma distribution function with the same mode but lower shape parameter, in  
 715 which  $k = 40$  and  $\theta = 0.112$ . The reciprocal of the new gamma distribution function was taken as the weighting factor. As a  
 716 result, samples exhibiting high or low DMS concentrations are more likely to be selected, whereas those with intermediate

717 concentrations are less likely to be selected. We also controlled the  $F_{\text{coastal}}$  value of the resampled data equal to 9.7%. The data  
718 distribution of DMS concentrations after the resampling process is shown in Fig. S7c. The fraction of samples with DMS  
719 concentrations above 15 nM or below 0.3 nM is elevated to 15.0%. The 50,000 samples were then randomly split to a training  
720 set (80%) and a validation set (20%). Since there are duplicate samples in the resampled dataset, the random data split was  
721 conducted based on the original sample ID before resampling to ensure that there was no sample overlap between the training  
722 and validation sets.

723

## 724 Appendix C: The calculation of airmass exposure to DMS emission (AEDMS)

725 Here the AEDMS index followed the similar calculation of the air mass exposure to Chl *a* (AEC) in previous studies (Arnold  
726 et al., 2010; Park et al., 2018; Zhou et al., 2021). We adopted the similar approach presented in Zhou et al. (2021) by replacing  
727 the Chl *a* concentration with DMS flux, as shown in the following equation (A2):

$$728 \quad AEDMS = \frac{\sum_{i=0}^{72} DMS\ flux_i \cdot e^{-\frac{t_i}{72} \frac{600}{BLH}}}{\sum_{i=0}^{72} e^{-\frac{t_i}{72}}} \quad (A2)$$

729 Here *i* represents the *i*-th trajectory point of the 72-hour backward trajectory (0-th for the receptor point). *DMS flux<sub>i</sub>* represents  
730 the ~~mean~~-DMS flux ~~within a radius of 20 km at the location~~ of ~~the pixel where the~~ *i*-th trajectory point ~~locates~~. *DMS flux<sub>i</sub>* is  
731 set to zero if the point locates on land or the air mass pressure is below 850 hPa (usually in the free troposphere with little  
732 influence of surface emission). *t<sub>i</sub>* is the tracking time of the trajectory point (unit: hour) and  $e^{-\frac{t_i}{72}}$  is the weighting factor to  
733 assign higher values for regions closer to the receptor point. To better connect with the atmospheric concentrations in the  
734 marine boundary layer, the normalization by boundary layer height (BLH) is added by the  $\frac{600}{BLH}$  term. The BLH below 50 m is  
735 replaced by 50 m.

## 736 Author contributions.

737 SZ and YC designed the research. SZ, FW, ZX, and KY collected the data and did the data preprocessing. SZ implemented  
738 the model development and performed the simulation with assistance from GY, HZ, and YZ. SH, HH, AW, and LP provided  
739 the measurement data of atmospheric MSA over the Atlantic Ocean. SZ conducted the data analysis and visualization with  
740 advice from YC and XG. SZ and YC wrote the manuscript with inputs from all authors.

## 741 Competing interests.

742 The authors declare that they have no conflict of interest.

743 **Acknowledgements.**

744 We greatly thank National Oceanic and Atmospheric Administration's Pacific Marine Environmental Laboratory for  
745 maintaining the Global Surface Seawater DMS Database. We acknowledge ~~Dr. Chenzhao Li for sharing the code of global~~  
746 ~~sensitivity analysis and~~ Dr. Martin Johnson for sharing the code of DMS transfer velocity calculation. We also thank Dr. Rich  
747 Pawlowicz for developing and sharing the M\_Map toolbox for Matlab (<https://www.eoas.ubc.ca/~rich/map.html>), which was  
748 used in the mapping of this study. XG was supported by the Research Center for Industries of the Future (RCIF) at Westlake  
749 University and Westlake University Education Foundation.

750 **Financial support.**

751 This work is jointly supported by Natural Science Foundation of Shanghai (22ZR1403800), National Key Research and  
752 Development Program of China (2016YFA0601304), and National Natural Science Foundation of China (41775145).

753

754 **References**

755 Abdar, M., Pourpanah, F., Hussain, S., Rezazadegan, D., Liu, L., Ghavamzadeh, M., Fieguth, P., Cao, X., Khosravi, A.,  
756 Acharya, U. R., Makarenkov, V., and Nahavandi, S.: A review of uncertainty quantification in deep learning: Techniques,  
757 applications and challenges, *Information Fusion*, 76, 243-297, 10.1016/j.inffus.2021.05.008, 2021.

758 Alcolombri, U., Ben-Dor, S., Feldmesser, E., Levin, Y., Tawfik, D. S., and Vardi, A.: Identification of the algal dimethyl  
759 sulfide-releasing enzyme: a missing link in the marine sulfur cycle, *Science*, 348, 1466-1469, 2015.

760 Andreae, M. O.: Ocean-Atmosphere Interactions in the Global Biogeochemical Sulfur Cycle, *Mar. Chem.*, 30, 1-29, Doi  
761 10.1016/0304-4203(90)90059-L, 1990.

762 Arnold, S. R., Spracklen, D. V., Gebhardt, S., Custer, T., Williams, J., Peek, I., and Alvain, S.: Relationships between  
763 atmospheric organic compounds and air-mass exposure to marine biology, *Environ. Chem.*, 7, 232-241, 10.1071/en09144,  
764 2010.

765 Aurin, D. A., and Dierssen, H. M.: Advantages and limitations of ocean color remote sensing in CDOM-dominated, mineral-  
766 rich coastal and estuarine waters, *Remote Sensing of Environment*, 125, 181-197, 10.1016/j.rse.2012.07.001, 2012.

767 Barnes, I., Hjorth, J., and Mihalopoulos, N.: Dimethyl sulfide and dimethyl sulfoxide and their oxidation in the atmosphere,  
768 *Chem. Rev.*, 106, 940-975, 10.1021/cr020529+, 2006.

769 Bates, T. S., Calhoun, J. A., and Quinn, P. K.: Variations in the Methanesulfonate to Sulfate Molar Ratio in Submicrometer  
770 Marine Aerosol-Particles over the South-Pacific Ocean, *J. Geophys. Res.-Atmos.*, 97, 9859-9865, 10.1029/92JD00411, 1992.

771 Beale, R., Johnson, M., Liss, P. S., and Nightingale, P. D.: Air-Sea Exchange of Marine Trace Gases, in: *Treatise on*  
772 *Geochemistry* (Second Edition), edited by: Holland, H. D., and Turekian, K. K., 2, Elsevier, Oxford, 53-92, 2014.

773 Behrenfeld, M. J., Moore, R. H., Hostetler, C. A., Graff, J., Gaube, P., Russell, L. M., Chen, G., Doney, S. C., Giovannoni, S.,  
774 Liu, H., Proctor, C., Bolaños, L. M., Baetge, N., Davie-Martin, C., Westberry, T. K., Bates, T. S., Bell, T. G., Bidle, K. D.,  
775 Boss, E. S., Brooks, S. D., Cairns, B., Carlson, C., Halsey, K., Harvey, E. L., Hu, C., Karp-Boss, L., Kleb, M., Menden-Deuer,  
776 S., Morison, F., Quinn, P. K., Scarino, A. J., Anderson, B., Chowdhary, J., Crosbie, E., Ferrare, R., Hair, J. W., Hu, Y., Janz,  
777 S., Redemann, J., Saltzman, E., Shook, M., Siegel, D. A., Wisthaler, A., Martin, M. Y., and Ziemb, L.: The North Atlantic  
778 Aerosol and Marine Ecosystem Study (NAAMES): Science Motive and Mission Overview, *Front. Mar. Sci.*, 6,  
779 10.3389/fmars.2019.00122, 2019.

780 Bell, T. G., Porter, J. G., Wang, W.-L., Lawler, M. J., Boss, E., Behrenfeld, M. J., and Saltzman, E. S.: Predictability of  
781 Seawater DMS During the North Atlantic Aerosol and Marine Ecosystem Study (NAAMES), *Front. Mar. Sci.*, 7, 596763,  
782 10.3389/fmars.2020.596763, 2021.

783 Belviso, S., Bopp, L., Moulin, C., Orr, J. C., Anderson, T. R., Aumont, O., Chu, S., Elliott, S., Maltrud, M. E., and Simó, R.:  
784 Comparison of global climatological maps of sea surface dimethyl sulfide, *Glob. Biogeochem. Cycles*, 18,  
785 10.1029/2003gb002193, 2004a.

786 Belviso, S., Moulin, C., Bopp, L., and Stefels, J.: Assessment of a global climatology of oceanic dimethylsulfide (DMS)  
787 concentrations based on SeaWiFS imagery (1998-2001), *Canadian Journal of Fisheries and Aquatic Sciences*, 61, 804-816,  
788 10.1139/f04-001, 2004b.

789 Belviso, S., Masotti, I., Tagliabue, A., Bopp, L., Brockmann, P., Fichot, C., Caniaux, G., Prieur, L., Ras, J., Uitz, J., Loisel,  
790 H., Dessailly, D., Alvain, S., Kasamatsu, N., and Fukuchi, M.: DMS dynamics in the most oligotrophic subtropical zones of  
791 the global ocean, *Biogeochemistry*, 110, 215-241, 10.1007/s10533-011-9648-1, 2011.

792 Bergen, K. J., Johnson, P. A., de Hoop, M. V., and Beroza, G. C.: Machine learning for data-driven discovery in solid Earth  
793 geoscience, *Science*, 363, eaau0323, 10.1126/science.aau0323, 2019.

794 Carslaw, K. S., Lee, L. A., Reddington, C. L., Pringle, K. J., Rap, A., Forster, P. M., Mann, G. W., Spracklen, D. V.,  
795 Woodhouse, M. T., Regayre, L. A., and Pierce, J. R.: Large contribution of natural aerosols to uncertainty in indirect forcing,  
796 *Nature*, 503, 67-71, 10.1038/nature12674, 2013.

797 Charlson, R. J., Lovelock, J. E., Andreae, M. O., and Warren, S. G.: Oceanic phytoplankton, atmospheric sulphur, cloud  
798 albedo and climate, *Nature*, 326, 655-661, 10.1038/326655a0, 1987.

799 Chawla, N. V., Bowyer, K. W., Hall, L. O., and Kegelmeyer, W. P.: SMOTE: synthetic minority over-sampling technique,  
800 *Journal of artificial intelligence research*, 16, 321-357, 2002.

801 Chen, Q., Sherwen, T., Evans, M., and Alexander, B.: DMS oxidation and sulfur aerosol formation in the marine troposphere:  
802 a focus on reactive halogen and multiphase chemistry, *Atmos. Chem. Phys.*, 18, 13617-13637, 10.5194/acp-18-13617-2018,  
803 2018.

804 Dubitzky, W., Granzow, M., and Berrar, D. P.: *Fundamentals of data mining in genomics and proteomics*, Springer Science  
805 & Business Media, 2007.

806 Forget, G., Campin, J.-M., Heimbach, P., Hill, C. N., Ponte, R. M., and Wunsch, C.: ECCO version 4: An integrated framework  
807 for non-linear inverse modeling and global ocean state estimation, *Geosci. Model Dev.*, 8, 3071-3104, 2015.

808 Friedland, K. D., Mouw, C. B., Asch, R. G., Ferreira, A. S. A., Henson, S., Hyde, K. J. W., Morse, R. E., Thomas, A. C., and  
809 Brady, D. C.: Phenology and time series trends of the dominant seasonal phytoplankton bloom across global scales, *Global  
810 Ecology and Biogeography*, 27, 551-569, 10.1111/geb.12717, 2018.

811 Fung, K. M., Heald, C. L., Kroll, J. H., Wang, S., Jo, D. S., Gettelman, A., Lu, Z., Liu, X., Zaveri, R. A., Apel, E. C., Blake,  
812 D. R., Jimenez, J. L., Campuzano-Jost, P., Veres, P. R., Bates, T. S., Shilling, J. E., and Zawadowicz, M.: Exploring dimethyl  
813 sulfide (DMS) oxidation and implications for global aerosol radiative forcing, *Atmos. Chem. Phys.*, 22, 1549-1573,  
814 10.5194/acp-22-1549-2022, 2022.

815 Galí, M., Devred, E., Levasseur, M., Royer, S.-J., and Babin, M.: A remote sensing algorithm for planktonic  
816 dimethylsulfoniopropionate (DMSP) and an analysis of global patterns, *Remote Sensing of Environment*, 171, 171-184,  
817 10.1016/j.rse.2015.10.012, 2015.

818 Galí, M., and Simó, R.: A meta-analysis of oceanic DMS and DMSP cycling processes: Disentangling the summer paradox,  
819 *Glob. Biogeochem. Cycles*, 29, 496-515, 10.1002/2014gb004940, 2015.

820 Galí, M., Levasseur, M., Devred, E., Simó, R., and Babin, M.: Sea-surface dimethylsulfide (DMS) concentration from satellite  
821 data at global and regional scales, *Biogeosciences*, 15, 3497-3519, 10.5194/bg-15-3497-2018, 2018.

822 Galí, M., Devred, E., Babin, M., and Levasseur, M.: Decadal increase in Arctic dimethylsulfide emission, *P. Natl. Acad. Sci.  
823 USA*, 116, 19311-19317, 10.1073/pnas.1904378116, 2019.

824 Garnesson, P., Mangin, A., Fanton d'Andon, O., Demaria, J., and Bretagnon, M.: The CMEMS GlobColour chlorophyll a  
825 product based on satellite observation: Multi-sensor merging and flagging strategies, *Ocean Science*, 15, 819-830, 2019.

826 Haibo, H., Yang, B., Garcia, E. A., and Shutao, L.: ADASYN: Adaptive synthetic sampling approach for imbalanced learning,  
827 2008 IEEE International Joint Conference on Neural Networks (IEEE World Congress on Computational Intelligence), 2008,  
828 1322-1328.

829 Hoffmann, E. H., Tilgner, A., Schroedner, R., Bräuer, P., Wolke, R., and Herrmann, H.: An advanced modeling study on the  
830 impacts and atmospheric implications of multiphase dimethyl sulfide chemistry, *P. Natl. Acad. Sci. USA*, 113, 11776-11781,  
831 10.1073/pnas.1606320113, 2016.

832 Holder, C., Gnanadesikan, A., and Aude-Pradal, M.: Using neural network ensembles to separate ocean biogeochemical and  
833 physical drivers of phytoplankton biogeography in Earth system models, *Geosci. Model Dev.*, 15, 1595-1617, 10.5194/gmd-  
834 15-1595-2022, 2022.

835 Hopkins, F. E., Turner, S. M., Nightingale, P. D., Steinke, M., Bakker, D., and Liss, P. S.: Ocean acidification and marine  
836 trace gas emissions, *P. Natl. Acad. Sci. USA*, 107, 760-765, 10.1073/pnas.0907163107, 2010.

837 Hopkins, F. E., Archer, S. D., Bell, T. G., Suntharalingam, P., and Todd, J. D.: The biogeochemistry of marine dimethylsulfide,  
838 *Nature Reviews Earth & Environment*, 4, 361-376, 10.1038/s43017-023-00428-7, 2023.

839 Huang, B., Liu, C., Freeman, E., Graham, G., Smith, T., and Zhang, H.-M.: Assessment and Intercomparison of NOAA Daily  
840 Optimum Interpolation Sea Surface Temperature (DOISST) Version 2.1, *Journal of Climate*, 34, 7421-7441, 10.1175/jcli-d-  
841 21-0001.1, 2021.

842 Huang, S., Poulain, L., van Pinxteren, D., van Pinxteren, M., Wu, Z., Herrmann, H., and Wiedensohler, A.: Latitudinal and  
843 Seasonal Distribution of Particulate MSA over the Atlantic using a Validated Quantification Method with HR-ToF-AMS,  
844 *Environ. Sci. Technol.*, 51, 418-426, 10.1021/acs.est.6b03186, 2016.

845 Hulswar, S., Simó, R., Galí, M., Bell, T. G., Lana, A., Inamdar, S., Halloran, P. R., Manville, G., and Mahajan, A. S.: Third  
846 revision of the global surface seawater dimethyl sulfide climatology (DMS-Rev3), *Earth System Science Data*, 14, 2963-2987,  
847 10.5194/essd-14-2963-2022, 2022.

848 Humphries, G. R. W., Deal, C. J., Elliott, S., and Huettmann, F.: Spatial predictions of sea surface dimethylsulfide  
849 concentrations in the high arctic, *Biogeochemistry*, 110, 287-301, 2012.

850 Johnson, M. T.: A numerical scheme to calculate temperature and salinity dependent air-water transfer velocities for any gas,  
851 *Ocean Science*, 6, 913-932, 10.5194/os-6-913-2010, 2010.

852 Keller, M. D., Bellows, W. K., and Guillard, R. R.: Dimethyl sulfide production in marine phytoplankton, in: *Biogenic Sulfur*  
853 in the Environment, edited by: Saltzman, E. S., and Cooper, W. J., ACS Publications, 1989.

854 Kettle, A. J., Andreae, M. O., Amouroux, D., Andreae, T. W., Bates, T. S., Berresheim, H., Bingemer, H., Boniforti, R., Curran,  
855 M. A. J., DiTullio, G. R., Helas, G., Jones, G. B., Keller, M. D., Kiene, R. P., Leck, C., Levasseur, M., Malin, G., Maspero,  
856 M., Matrai, P., McTaggart, A. R., Mihalopoulos, N., Nguyen, B. C., Novo, A., Putaud, J. P., Rapsomanikis, S., Roberts, G.,  
857 Schebeske, G., Sharma, S., Simo, R., Staubes, R., Turner, S., and Uher, G.: A global database of sea surface dimethylsulfide  
858 (DMS) measurements and a procedure to predict sea surface DMS as a function of latitude, longitude, and month, *Glob.*  
859 *Biogeochem. Cycles*, 13, 399-444, 10.1029/1999gb900004, 1999.

860 Kloster, S., Feichter, J., Maier-Reimer, E., Six, K. D., Stier, P., and Wetzel, P.: DMS cycle in the marine ocean-atmosphere  
861 system—a global model study, *Biogeosciences*, 3, 29-51, 2006.

862 Lana, A., Bell, T. G., Simó, R., Vallina, S. M., Ballabriga-Poy, J., Kettle, A. J., Dachs, J., Bopp, L., Saltzman, E. S., Stefels,  
863 J., Johnson, J. E., and Liss, P. S.: An updated climatology of surface dimethylsulfide concentrations and emission fluxes in the  
864 global ocean, *Glob. Biogeochem. Cycles*, 25, GB1004, 10.1029/2010gb003850, 2011.

865 Li, H., Zhou, S., Zhu, Y., Zhang, R., Wang, F., Bao, Y., and Chen, Y.: Atmospheric Deposition Promotes Relative Abundances  
866 of High-Dimethylsulfoniopropionate Producers in the Western North Pacific, *Geophys. Res. Lett.*, 48, e2020GL092077,  
867 10.1029/2020GL092077, 2021.

868 Longhurst, A. R.: *Ecological Geography of the Sea*, Academic Press, 1998.

869 Lovelock, J. E., Maggs, R. J., and Rasmussen, R. A.: Atmospheric Dimethyl Sulphide and the Natural Sulphur Cycle, *Nature*,  
870 237, 452-453, 10.1038/237452a0, 1972.

871 Mansour, K., Decesari, S., Ceburnis, D., Ovadnevaite, J., and Rinaldi, M.: Machine learning for prediction of daily sea surface  
872 dimethylsulfide concentration and emission flux over the North Atlantic Ocean (1998-2021), *Sci. Total. Environ.*, 871, 162123,  
873 10.1016/j.scitotenv.2023.162123, 2023.

874 Masson-Delmotte, V., Zhai, P., Pirani, A., Connors, S. L., Péan, C., Berger, S., Caud, N., Chen, Y., Goldfarb, L., Gomis, M.  
875 I., Huang, M., Leitzell, K., Lonnoy, E., Matthews, J. B. R., Maycock, T. K., Waterfield, T., Yelekçi, O., Yu, R., and Zhou, R.  
876 e.: *IPCC, 2021: Climate Change 2021: The Physical Science Basis. Contribution of Working Group I to the Sixth Assessment  
877 Report of the Intergovernmental Panel on Climate Change*, 2021.

878 McCoy, D. T., Burrows, S. M., Wood, R., Grosvenor, D. P., Elliott, S. M., Ma, P. L., Rasch, P. J., and Hartmann, D. L.: Natural  
879 aerosols explain seasonal and spatial patterns of Southern Ocean cloud albedo, *Science Advances*, 1, e1500157,  
880 10.1126/sciadv.1500157, 2015.

881 McNabb, B. J., and Tortell, P. D.: Improved prediction of dimethyl sulfide (DMS) distributions in the northeast subarctic  
882 Pacific using machine-learning algorithms, *Biogeosciences*, 19, 1705-1721, 10.5194/bg-19-1705-2022, 2022.

883 McNabb, B. J., and Tortell, P. D.: Oceanographic controls on Southern Ocean dimethyl sulfide distributions revealed by  
884 machine learning algorithms, *Limnology and Oceanography*, 68, 616-630, 10.1002/lo.12298, 2023.

885 McParland, E. L., and Levine, N. M.: The role of differential DMSP production and community composition in predicting  
886 variability of global surface DMSP concentrations, *Limnol. Oceanogr.*, 64, 757-773, 10.1002/lo.11076, 2018.

887 Moradkhani, H., DeChant, C. M., and Sorooshian, S.: Evolution of ensemble data assimilation for uncertainty quantification  
888 using the particle filter-Markov chain Monte Carlo method, *Water Resources Research*, 48, 10.1029/2012wr012144, 2012.

889 Nightingale, P. D., Malin, G., Law, C. S., Watson, A. J., Liss, P. S., Liddicoat, M. I., Boutin, J., and Upstill-Goddard, R. C.:  
890 In situ evaluation of air-sea gas exchange parameterizations using novel conservative and volatile tracers, *Glob. Biogeochem.  
891 Cycles*, 14, 373-387, 10.1029/1999gb900091, 2000.

892 Novak, G. A., Fite, C. H., Holmes, C. D., Veres, P. R., Neuman, J. A., Faloona, I., Thornton, J. A., Wolfe, G. M., Vermeuel,  
893 M. P., Jernigan, C. M., Peischl, J., Ryerson, T. B., Thompson, C. R., Bourgeois, I., Warneke, C., Gkatzelis, G. I., Coggon, M.  
894 M., Sekimoto, K., Bui, T. P., Dean-Day, J., Diskin, G. S., DiGangi, J. P., Nowak, J. B., Moore, R. H., Wiggins, E. B., Winstead,  
895 E. L., Robinson, C., Thornhill, K. L., Sanchez, K. J., Hall, S. R., Ullmann, K., Dollner, M., Weinzierl, B., Blake, D. R., and  
896 Bertram, T. H.: Rapid cloud removal of dimethyl sulfide oxidation products limits SO<sub>2</sub> and cloud condensation nuclei  
897 production in the marine atmosphere, *P. Natl. Acad. Sci. USA*, 118, e2110472118, 10.1073/pnas.2110472118, 2021.

898 Omori, Y., Tanimoto, H., Inomata, S., Wada, S., Thume, K., and Pohnert, G.: Enhancement of dimethylsulfide production by  
899 anoxic stress in natural seawater, *Geophys. Res. Lett.*, 42, 4047-4053, 10.1002/2015gl063546, 2015.

900 Osman, M. B., Das, S. B., Trusel, L. D., Evans, M. J., Fischer, H., Grieman, M. M., Kipfstuhl, S., McConnell, J. R., and  
901 Saltzman, E. S.: Industrial-era decline in subarctic Atlantic productivity, *Nature*, 569, 551-555, 10.1038/s41586-019-1181-8,  
902 2019.

903 Park, K.-T., Lee, K., Kim, T.-W., Yoon, Y. J., Jang, E.-H., Jang, S., Lee, B.-Y., and Hermansen, O.: Atmospheric DMS in the  
904 Arctic Ocean and Its Relation to Phytoplankton Biomass, *Glob. Biogeochem. Cycles*, 32, 351-359, 10.1002/2017gb005805,  
905 2018.

906 Park, K. T., Yoon, Y. J., Lee, K., Tunved, P., Krejci, R., Ström, J., Jang, E., Kang, H. J., Jang, S., Park, J., Lee, B. Y., Traversi,  
907 R., Becagli, S., and Hermansen, O.: Dimethyl Sulfide-Induced Increase in Cloud Condensation Nuclei in the Arctic  
908 Atmosphere, *Glob. Biogeochem. Cycles*, 35, e2021GB006969, 10.1029/2021gb006969, 2021.

909 Qu, B., Gabric, A. J., Zeng, M., and Lu, Z.: Dimethylsulfide model calibration in the Barents Sea using a genetic algorithm  
910 and neural network, *Environ. Chem.*, 13, 413-424, 10.1071/EN14264, 2016.

911 Quinn, P. K., and Bates, T. S.: The case against climate regulation via oceanic phytoplankton sulphur emissions, *Nature*, 480,  
912 51-56, 10.1038/nature10580, 2011.

913 Quinn, P. K., Coffman, D. J., Johnson, J. E., Upchurch, L. M., and Bates, T. S.: Small fraction of marine cloud condensation  
914 nuclei made up of sea spray aerosol, *Nat. Geosci.*, 10, 674-679, 10.1038/ngeo3003, 2017.

915 Reichstein, M., Camps-Valls, G., Stevens, B., Jung, M., Denzler, J., Carvalhais, N., and Prabhat: Deep learning and process  
916 understanding for data-driven Earth system science, *Nature*, 566, 195-204, 10.1038/s41586-019-0912-1, 2019.

917 Saltzman, E. S., Savoie, D. L., Zika, R. G., and Prospero, J. M.: Methane sulfonic acid in the marine atmosphere, *J. Geophys.  
918 Res.*, 88, 10897, 10.1029/JC088iC15p10897, 1983.

919 Savoie, D. L., Arimoto, R., Keene, W. C., Prospero, J. M., Duce, R. A., and Galloway, J. N.: Marine biogenic and  
920 anthropogenic contributions to non-sea-salt sulfate in the marine boundary layer over the North Atlantic Ocean, *J. Geophys.  
921 Res.*, 107, 4356, 10.1029/2001jd000970, 2002.

922 Screen, J. A., Deser, C., and Simmonds, I.: Local and remote controls on observed Arctic warming, *Geophys. Res. Lett.*, 39,  
923 L10709, 10.1029/2012gl051598, 2012.

924 Serreze, M. C., and Barry, R. G.: Processes and impacts of Arctic amplification: A research synthesis, *Global and planetary  
925 change*, 77, 85-96, 2011.

926 Sheng, J.-X., Weisenstein, D. K., Luo, B.-P., Rozanov, E., Stenke, A., Anet, J., Bingemer, H., and Peter, T.: Global atmospheric  
927 sulfur budget under volcanically quiescent conditions: Aerosol-chemistry-climate model predictions and validation, *J.  
928 Geophys. Res.-Atmos.*, 120, 256-276, 10.1002/2014jd021985, 2015.

929 Sigmund, G., Gharasoo, M., Hüffer, T., and Hofmann, T.: Deep Learning Neural Network Approach for Predicting the  
930 Sorption of Ionizable and Polar Organic Pollutants to a Wide Range of Carbonaceous Materials, *Environ. Sci. Technol.*, 54,  
931 4583-4591, 10.1021/acs.est.9b06287, 2020.

932 Simó, R., and Pedrós-Alió, C.: Role of vertical mixing in controlling the oceanic production of dimethyl sulphide, *Nature*, 402,  
933 396-399, 10.1038/46516, 1999a.

934 Simó, R., and Pedrós-Alió, C.: Short-term variability in the open ocean cycle of dimethylsulfide, *Glob. Biogeochem. Cycles*,  
935 13, 1173-1181, 10.1029/1999gb900081, 1999b.

936 Simó, R., and Dachs, J.: Global ocean emission of dimethylsulfide predicted from biogeophysical data, *Glob. Biogeochem. Cycles*, 16, 1078, 10.1029/2001gb001829, 2002.

938 Six, K. D., Kloster, S., Ilyina, T., Archer, S. D., Zhang, K., and Maier-Reimer, E.: Global warming amplified by reduced sulphur fluxes as a result of ocean acidification, *Nat. Clim. Change*, 3, 975-978, 10.1038/nclimate1981, 2013.

940 Stefels, J.: Physiological aspects of the production and conversion of DMSP in marine algae and higher plants, *J. Sea. Res.*, 43, 183-197, 2000.

942 Stefels, J., Steinke, M., Turner, S., Malin, G., and Belviso, S.: Environmental constraints on the production and removal of the climatically active gas dimethylsulphide (DMS) and implications for ecosystem modelling, *Biogeochemistry*, 83, 245-275, 10.1007/s10533-007-9091-5, 2007.

944 Stein, A. F., Draxler, R. R., Rolph, G. D., Stunder, B. J. B., Cohen, M. D., and Ngan, F.: NOAA's HYSPLIT Atmospheric Transport and Dispersion Modeling System, *Bull. Am. Meteorol. Soc.*, 96, 2059-2077, 10.1175/bams-d-14-00110.1, 2015.

946 Steiner, N. S., Robert, M., Arychuk, M., Levasseur, M. L., Merzouk, A., Peña, M. A., Richardson, W. A., and Tortell, P. D.: Evaluating DMS measurements and model results in the Northeast subarctic Pacific from 1996–2010, *Biogeochemistry*, 110, 269-285, 10.1007/s10533-011-9669-9, 2011.

948 Sunda, W., Kieber, D., Kiene, R., and Huntsman, S.: An antioxidant function for DMSP and DMS in marine algae, *Nature*, 418, 317-320, 2002.

950 Tesdal, J.-E., Christian, J. R., Monahan, A. H., and Salzen, K. v.: Evaluation of diverse approaches for estimating sea-surface DMS concentration and air-sea exchange at global scale, *Environ. Chem.*, 13, 390-412, 10.1071/EN14255, 2016.

952 Vallina, S. M., and Simó, R.: Strong relationship between DMS and the solar radiation dose over the global surface ocean, *Science*, 315, 506-508, 10.1126/science.1133680, 2007.

954 Vogt, M., Vallina, S. M., Buitenhuis, E. T., Bopp, L., and Le Quéré, C.: Simulating dimethylsulphide seasonality with the Dynamic Green Ocean Model PlankTOM5, *J. Geophys. Res.*, 115, 10.1029/2009jc005529, 2010.

956 Wang, S., Elliott, S., Maltrud, M., and Cameron-Smith, P.: Influence of explicit *Phaeocystis* parameterizations on the global distribution of marine dimethyl sulfide, *J. Geophys. Res.-Biogeosci.*, 120, 2158-2177, 10.1002/2015jg003017, 2015.

958 Wang, W.-L., Song, G., Primeau, F., Saltzman, E. S., Bell, T. G., and Moore, J. K.: Global ocean dimethyl sulfide climatology estimated from observations and an artificial neural network, *Biogeosciences*, 17, 5335-5354, 10.5194/bg-17-5335-2020, 2020.

960 Wood, R., Stemmler, J. D., Rémillard, J., and Jefferson, A.: Low-CCN concentration air masses over the eastern North Atlantic: Seasonality, meteorology, and drivers, *J. Geophys. Res. Atmos.*, 122, 1203-1223, 10.1002/2016jd025557, 2017.

962 Woolf, D. K.: Bubbles and their role in gas exchange, in: *The Sea Surface and Global Change*, edited by: Liss, P. S., and Duce, R. A., Cambridge University Press, Cambridge, 173-206, 1997.

964 Yang, B., Boss, E. S., Haëntjens, N., Long, M. C., Behrenfeld, M. J., Eveleth, R., and Doney, S. C.: Phytoplankton Phenology in the North Atlantic: Insights From Profiling Float Measurements, *Front. Mar. Sci.*, 7, 10.3389/fmars.2020.00139, 2020.

966 Yu, L., and Zhou, N.: Survey of imbalanced data methodologies, *arXiv preprint arXiv:2104.02240*, 2021.

970 Zhang, X. H., Liu, J., Liu, J., Yang, G., Xue, C. X., Curson, A. R. J., and Todd, J. D.: Biogenic production of DMSP and its  
971 degradation to DMS-their roles in the global sulfur cycle, *Sci. China Life Sci.*, 62, 1296-1319, 10.1007/s11427-018-9524-y,  
972 2019.

973 Zhao, J., Ma, W., Bilsback, K. R., Pierce, J. R., Zhou, S., Chen, Y., Yang, G., and Zhang, Y.: Simulating the radiative forcing  
974 of oceanic dimethylsulfide (DMS) in Asia based on machine learning estimates, *Atmos. Chem. Phys.*, 22, 9583-9600,  
975 10.5194/acp-22-9583-2022, 2022.

976 Zheng, G., Li, X., Zhang, R. H., and Liu, B.: Purely satellite data-driven deep learning forecast of complicated tropical  
977 instability waves, *Science Advances*, 6, eaba1482, 10.1126/sciadv.aba1482, 2020.

978 Zhou, S.: An artificial neural network ensemble model for sea surface DMS simulation, [v2v3.0](#), Zenodo [Data set],  
979 <https://doi.org/10.5281/zenodo.1239898510937598>, 2024

980 Zhou, S., Chen, Y., Huang, S., Gong, X., Yang, G., Zhang, H., Herrmann, H., Wiedensohler, A., Poulain, L., Zhang, Y., Wang,  
981 F., Xu, Z., and Yan, K.: A 20-year (1998-2017) global sea surface dimethyl sulfide gridded dataset with daily resolution,  
982 [v3v4.0](#), Zenodo [Data set], <https://doi.org/10.5281/zenodo.1187990040906101>, 2024.

983 Zhou, S., Chen, Y., Paytan, A., Li, H., Wang, F., Zhu, Y., Yang, T., Zhang, Y., and Zhang, R.: Non-Marine Sources Contribute  
984 to Aerosol Methanesulfonate Over Coastal Seas, *J. Geophys. Res.-Atmos.*, 126, e2021JD034960, 10.1029/2021jd034960,  
985 2021.

986 Zindler, C., Bracher, A., Marandino, C. A., Taylor, B., Torrecilla, E., Kock, A., and Bange, H. W.: Sulphur compounds,  
987 methane, and phytoplankton: interactions along a north-south transit in the western Pacific Ocean, *Biogeosciences*, 10, 3297-  
988 3311, 10.5194/bg-10-3297-2013, 2013.

989 Zindler, C., Marandino, C. A., Bange, H. W., Schütte, F., and Saltzman, E. S.: Nutrient availability determines dimethyl sulfide  
990 and isoprene distribution in the eastern Atlantic Ocean, *Geophys. Res. Lett.*, 41, 3181-3188, 10.1002/2014gl059547, 2014.

991